

# Parameters Variation and Flow Characteristics when CO<sub>2</sub> Displacing Brine in Four Micromodels Simulating Carbon Sequestration in Saline Aquifers

Changzhong Zhao<sup>1</sup>, Yi Zhang<sup>1</sup>, Ke Chen<sup>1</sup>, Lei Yuan<sup>1</sup>, Shezhan Liu<sup>1</sup>, Mingkun Chen<sup>1</sup>, and Yongchen Song<sup>1</sup>

<sup>1</sup>Dalian University of Technology

November 23, 2022

## Abstract

Two-phase flow of CO<sub>2</sub>/brine in porous media is critical to the capacity and safety of carbon sequestration into the brine aquifer. In order to provide valuable information and important theoretical basis for site selection and CO<sub>2</sub> injection, the microscopic visualization technology was employed in this study to conduct displacement experiments of CO<sub>2</sub>/brine at the pore scale. Four micromodels with different sizes and structures, five injection rates of CO<sub>2</sub> and six salinities of brine were used to study the effects of micromodel's structure and displacement pattern on two-phase flow. Several parameters including the differential pressure, contact angle, permeability, velocity field and force field were obtained by experimental measurement, image post-processing and theoretical analysis, and then these parameters' variation was investigated. Phenomena such as thin film, corner flow and Haines jump were also found during the displacement. Although brine could be completely displaced by CO<sub>2</sub> in the capillary duct, the backflow of wetting phase would occur at low injection rate. Phenomena different from the theoretical analysis also occurred in pore doublet models: some brine was residual in the homogeneous pore doublet model at low injection rate, while the heterogeneous pore doublet model was fully occupied by CO<sub>2</sub> at high injection rate. These phenomena are very useful for two-phase flow, and multiple factors need to be comprehensively considered to determine the operating conditions of CO<sub>2</sub> storage into the brine aquifer.

1     **Parameters Variation and Flow Characteristics when CO<sub>2</sub> Displacing Brine in Four**  
2             **Micromodels Simulating Carbon Sequestration in Saline Aquifers**

3     **Changzhong Zhao<sup>1</sup>, Yi Zhang<sup>1\*</sup>, Ke Chen<sup>1</sup>, Lei Yuan<sup>1</sup>, Shezhan Liu<sup>1</sup>, Mingkun Chen<sup>1</sup>,**  
4     **Yongchen Song<sup>1</sup>**

5     <sup>1</sup>Key Laboratory of Ocean Energy Utilization and Energy Conservation of Ministry of  
6     Education, School of Energy and Power Engineering, Dalian University of Technology, Dalian  
7     116024, China.

8     **Key Points:**

- 9             • Structure, flow rate and salinity all affected the amount and safety of CO<sub>2</sub> captured during  
10            the sequestration in saline aquifers  
11            • The displacement pattern was not constant during the flow through theoretical analysis  
12            and experimental result of velocity and force field  
13            • Back flow, corner flow and more intense Haines jump were found when CO<sub>2</sub> displaced  
14            brine in different displacement patterns.

## 15 Abstract

16 Two-phase flow of CO<sub>2</sub>/brine in porous media is critical to the capacity and safety of carbon  
17 sequestration into the brine aquifer. In order to provide valuable information and important  
18 theoretical basis for site selection and CO<sub>2</sub> injection, the microscopic visualization technology  
19 was employed in this study to conduct displacement experiments of CO<sub>2</sub>/brine at the pore scale.  
20 Four micromodels with different sizes and structures, five injection rates of CO<sub>2</sub> and six  
21 salinities of brine were used to study the effects of micromodel's structure and displacement  
22 pattern on two-phase flow. Several parameters including the differential pressure, contact angle,  
23 permeability, velocity field and force field were obtained by experimental measurement, image  
24 post-processing and theoretical analysis, and then these parameters' variation was investigated.  
25 Phenomena such as thin film, corner flow and Haines jump were also found during the  
26 displacement. Although brine could be completely displaced by CO<sub>2</sub> in the capillary duct, the  
27 backflow of wetting phase would occur at low injection rate. Phenomena different from the  
28 theoretical analysis also occurred in pore doublet models: some brine was residual in the  
29 homogeneous pore doublet model at low injection rate, while the heterogeneous pore doublet  
30 model was fully occupied by CO<sub>2</sub> at high injection rate. These phenomena are very useful for  
31 two-phase flow, and multiple factors need to be comprehensively considered to determine the  
32 operating conditions of CO<sub>2</sub> storage into the brine aquifer.

## 33 1 Introduction

34 Fluid flow in porous media has many applications (Berejnov et al., 2008), such as oil and  
35 gas resource recovery, groundwater contamination, CO<sub>2</sub> geological storage (CGS) (Patmonoaji et  
36 al., 2020). As an important technology of CGS, carbon storage in the brine aquifer can achieve  
37 massive CO<sub>2</sub> storage and thus effectively control the global warming. The two-phase flow of  
38 CO<sub>2</sub>/brine in the formation is a key factor for the storage capacity and security of the brine  
39 aquifer (Morais et al., 2016).

40 At present, a large number of experimental and simulation studies on CO<sub>2</sub>/brine two-  
41 phase flow have been conducted. Pore structure is one of the main factors affecting flow  
42 behavior in porous media (Gaol et al., 2020). CO<sub>2</sub> displacement of brine in real cores is carried  
43 out by the conventional High-Temperature-High-Pressure (HTHP) experimental system to study  
44 the effects of temperature, pressure, injection flow rate and salinity of brine on the permeability  
45 and displacement efficiency (Bai et al., 2020; Chang et al., 2014; Chen et al., 2016). However,  
46 the understanding of the transport mechanism is limited by the difficulty of monitoring fluid flow  
47 in opaque media (Wu et al., 2012). With the development of technology, this problem is  
48 overcome by non-invasive image techniques such as optical imaging, gamma imaging,  
49 synchrotron X-ray microtomography and magnetic resonance imaging, which allow the  
50 visualization study of two-phase flow in real porous media at the core or pore scale. But there are  
51 still some problems with these techniques like expensive equipment, complex operation and  
52 limited temporal resolution, so that some subtle changes are easily overlooked (Werth et al.,  
53 2010).

54 The visualization technique of combining a microscope with a camera can  
55 simultaneously achieve high-resolution temporal and spatial measurement by adjusting the  
56 frames per second (fps) of camera and the magnification of microscope, and has been  
57 increasingly applied to the study of CO<sub>2</sub>/brine flows in recent years. Chang et al. from Lawrence  
58 Berkeley National Laboratory have comprehensively and systematically studied the CO<sub>2</sub>/brine

59 displacement and imbibition under formation conditions using many micromodels with different  
60 structures, including homogeneous structure, real core structure and even 2.5-D structure, to  
61 identify the non-equilibrium dissolution, diffusion, two-phase distribution, storage capacity, and  
62 flow mechanism (Chang et al., 2017; Chang et al., 2019; Chang et al., 2020; Chang et al., 2016).  
63 On the other hand, Jafari et al. from Louisiana State University mainly focused on the micro-  
64 scale contact angles using the inhomogeneous micromodel at room temperature and high  
65 pressure during the process of CO<sub>2</sub> displacing brine (Jafari and Jung, 2017; 2019). Kazemifar et  
66 al. from the University of Illinois at Urbana-Champaign used the micro-PIV technique to  
67 describe the velocity field of CO<sub>2</sub>/brine in the homogeneous micromodel under high temperature  
68 and pressure (Kazemifar et al., 2015; 2016). Nevertheless, some phenomena on the macroscopic  
69 scale have not been fully explained. Some special phenomena have been found on the  
70 microscopic scale, which need to be supplemented by more experiments and simulations. So, this  
71 study aims to conduct the CO<sub>2</sub> displacement of brine in four micromodels to provide the  
72 microscopic theoretical basis for flow phenomena based on the fields of velocity and force.

73 As early as the 1980s, visualization techniques have been used to study two-phase flow in  
74 simple micromodels. Chatzis et al. investigated the flow mechanism when displacement and  
75 imbibition of water/oil occurred in the pore doublet model in 1983 (Chatzis and Dullien, 1983).  
76 Since then, Lenormand et al. have performed lots of displacement and imbibition experiments in  
77 the capillary duct and network of capillary ducts, mainly of air/oil, and proposed the classical  
78 flow pattern on the pore scale that laid the foundation for two-phase flow (R. Lenormand and  
79 Zarcone, 1985; R Lenormand et al., 1983; Roland Lenormand et al., 1987). Subsequently, Dong  
80 et al. observed the imbibition of five different fluid pairs in a capillary duct with the rectangular  
81 cross-section and investigated the effect of channel size and fluid viscosity on the percolation  
82 rate (M. Dong, 1995). In 2009, Zhu et al. measured the contact angle and velocity field of  
83 water/air in two different capillary ducts with circular and rectangular cross-sections,  
84 respectively, combined with the theoretical analysis (Zhu and Petkovic-Duran, 2009). These  
85 studies were only using the camera with fps less than 1. So, the temporal and spatial resolution of  
86 the two-phase flow was limited. To the best of our knowledge, there is only one research where  
87 the visualization technique with a microscope combined with a camera was used to study the  
88 CO<sub>2</sub> displacement of brine in the capillary duct. It is Sell et al. who investigated the effects of  
89 salinity and pressure on convection and diffusion when CO<sub>2</sub> was injected into the curved  
90 capillary duct to displace the brine in 2013 (Sell et al., 2013). Therefore, more experiments on  
91 displacement of CO<sub>2</sub>/brine in capillary duct or pore doublet model are needed to provide more  
92 adequate and complete mechanisms and phenomena for simulation calculations and engineering  
93 applications in the formation.

94 The main objective of this study is to complement the existing CO<sub>2</sub>/brine flow  
95 mechanisms and phenomena by improving the temporal and spatial resolution using fluorescence  
96 inverted microscopy combined with high-speed camera. Two capillary ducts with different  
97 widths and two pore doublet models with different structures were used to visualize the process  
98 of CO<sub>2</sub> displacing brine under different capillary numbers  $Ca$  and viscous ratios  $M$ . Contact  
99 angle  $\theta$ , residual brine saturation  $S_w$  and velocity field were obtained by image measurement. At  
100 the same time, CO<sub>2</sub> relative permeability  $K_{rg}$  and force field were obtained by experimental data  
101 combined with theoretical analysis. Finally, two-phase flow and some special phenomena in the  
102 capillary duct and the pore doublet model were described in detail, and relevant mechanisms  
103 were proposed using the obtained multiple parameters.

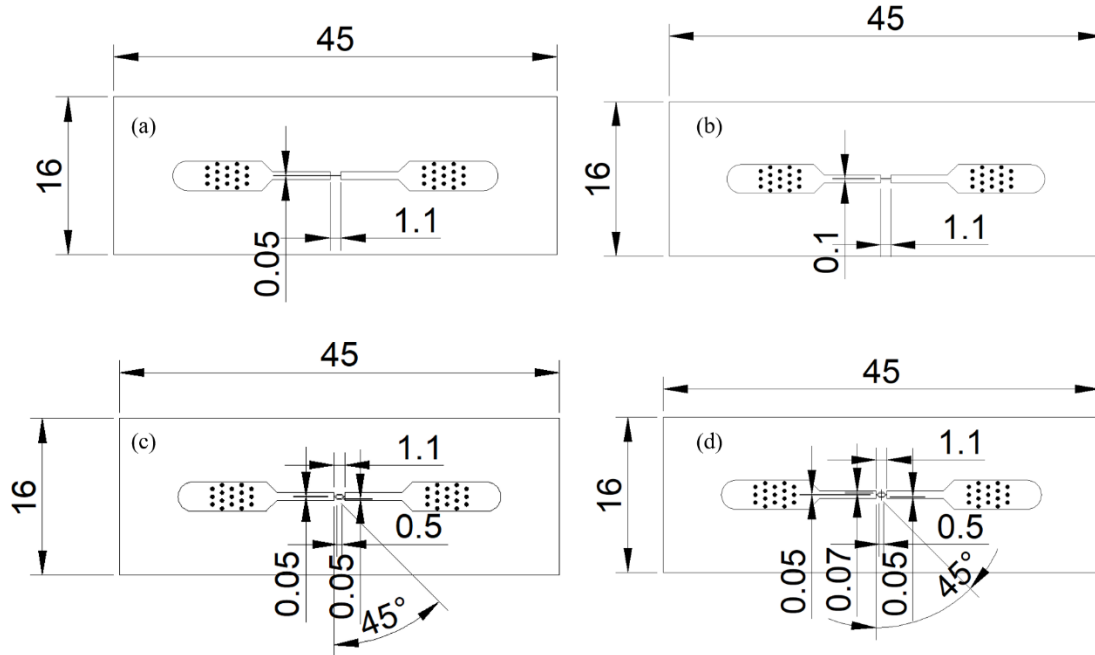
## 104 2 Materials and Methods

105 The size and connectivity of the pores and throats in the formation determine the  
 106 migration pathways and sequestration capacity of CO<sub>2</sub> in the brine aquifer. So, two capillary  
 107 ducts with different widths and two pore doublet models with different sizes were designed in  
 108 this study to simplify the structure of formation and then reveal the CO<sub>2</sub>/brine flow  
 109 characteristics at the microscopic scale.

### 110 2.1 Experimental materials and conditions

111 Four design diagrams of micromodels are shown in Fig. 1. Two pieces of glass, 45 mm in  
 112 length and 16 mm in width, were bonded together to form the micromodel that were made by  
 113 Wenhao Co., Ltd. using the laser etching. Through the contact angle measurement, all  
 114 micromodels in this study were hydrophilic. To mitigate the entrance/exit effect, two buffer  
 115 zones consisting of cylinders were added near the entrance and exit of the micromodel, and then  
 116 capillary conducts with 0.8 mm wide, 1.8 mm long were connected to the target area. The  
 117 studied area had a length  $l$  of 1.1 mm. Two capillary ducts, with widths  $w$  of 0.05 mm and 0.1  
 118 mm, respectively, had a high aspect ratio, which was closer to the structure of real core. Both  
 119 capillary ducts had the same  $w$  of 0.05 mm in the homogeneous pore doublet model, while the  $w$   
 120 of upper duct was 0.05 mm and the lower one was 0.07 mm in the heterogeneous pore doublet  
 121 model. The etching depth  $d$  of all micromodels in this study was 0.02 mm. The pore volumes  
 122 (PV) of four micromodels are shown in Table 1. All experiments were carried out at ambient  
 123 temperature and pressure (25°C, 0.1 MPa) in this study.

124



125

126 **Figure 1.** Design diagrams of four micromodels in mm, (a) the capillary duct with the  $w$  of 0.05  
 127 mm, (b) the capillary duct with the  $w$  of 0.1 mm, (c) the homogeneous pore doublet model, (d)  
 128 the heterogeneous pore doublet model.

129

130 The effects of injection flow rate and duct size on displacement were first investigated,  
 131 with CO<sub>2</sub> volumetric flow rate  $Q$  ranging from 0.002-0.1 ml/min, which was converted into the  
 132 bulk velocity  $v$  by

$$133 \quad v = \frac{Q}{A} \quad (1)$$

134 Where  $A$  is the cross-sectional area of capillary duct. Then,  $Ca$  under different conditions  
 135 could be calculated by

$$136 \quad Ca = \frac{\mu_2 v}{\gamma \cos \theta} \quad (2)$$

137 where  $\theta$  was obtained by averaging advancing contact angles for each experiment, which  
 138 were affected by several factors such as injection flow rate, micromodel structure and brine  
 139 salinity. And the measured average advancing contact angles are shown in Tables 1 and 2. The  
 140 viscosities  $\mu_1, \mu_2$  of pure water and CO<sub>2</sub> at ambient temperature and pressure were obtained as  
 141 0.8898 and 0.0149 mPa·s, respectively, based on the NIST database. Thus,  $M$  was obtained  
 142 through

$$143 \quad M = \frac{\mu_2}{\mu_1} \quad (3)$$

144  $\log M = -1.775$  in this study. The interfacial tension  $\gamma$  between CO<sub>2</sub> and pure water was  
 145 obtained using the empirical equation proposed by Li et al., (Li et al., 2013) and  $\gamma = 73.628$  mN/m.  
 146 The calculated  $\log Ca$  are shown in Table 1. Currently, Lenormand-Zhang phase diagram (Roland  
 147 Lenormand et al., 1987; Zhang et al., 2011) is often used to determine the pattern of  
 148 displacement or imbibition on the pore scale, and our distributions of  $\log M - \log Ca$  in this phase  
 149 diagram are shown in Fig. 2. The viscous force of wetting phase dominated in almost all  
 150 displacements, when the displacement pattern was viscous fingering. At lower injection rates of  
 151 0.002 and 0.005 ml/min, the displacement pattern became crossover where both capillary and  
 152 viscous forces dominated.

153

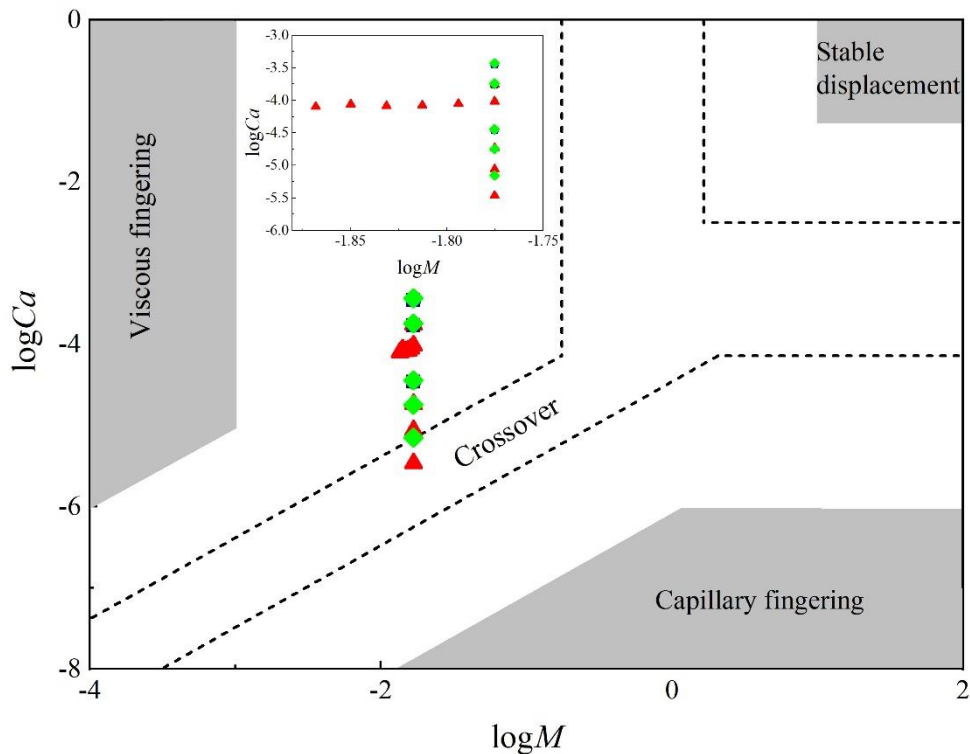
154 **Table 1.** Measured or calculated the bulk injection velocity  $v$ , capillary number  $\log Ca$ , contact  
 155 angle  $\theta$ , absolute permeability  $K$  and pore volume PV when CO<sub>2</sub> displaced pure water in  
 156 different micromodels with different volumetric injection flow rates  $Q$ .

$Q$ (ml/min)	0.05 mm wide capillary duct			0.1 mm wide capillary duct			Homogeneous pore doublet model			Heterogeneous pore doublet model		
	$v$ (m/s)	$\theta$ (°)	$\log Ca$	$v$ (m/s)	$\theta$ (°)	$\log Ca$	$v$ (m/s)	$\theta$ (°)	$\log Ca$	$v$ (m/s)	$\theta$ (°)	$\log Ca$
0.002	-	-	-	0.017	9.51	-5.465	-	-	-	0.033	16.08	-5.153
0.005	-	-	-	0.042	14.35	-5.059	-	-	-	0.083	18.80	-4.748
0.01	0.167	10.43	-4.464	0.083	23.05	-4.736	0.167	12.63	-4.460	0.167	19.81	-4.445
0.05	0.833	9.28	-3.766	0.417	28.41	-4.017	0.833	14.11	-3.759	0.833	20.39	-3.744
0.1	1.667	11.47	-3.462	0.833	14.67	-3.758	1.667	16.47	-3.453	1.667	24.11	-3.431
$K$ (D)	3.358			15.373			11.635			11.897		
PV ( $\mu$ L)	0.0011			0.0022			0.002736			0.002674		

157

158 The actual brine aquifer has a certain degree of mineralization, so the effect of brine  
 159 salinity on two phase flow was also studied with the salinity range of 0-2.5 mol/l in the 0.1 mm  
 160 wide capillary duct at the injection rate of 0.05 ml/min. The brine viscosity, interfacial tension  
 161 with CO<sub>2</sub> and contact angle were subsequently affected by salinity and these parameters and the  
 162 corresponding  $\log Ca$  and  $\log M$  are shown in Table 2. The  $\mu_1$  of brine was calculated by the  
 163 model proposed by Mao et al., (Mao and Duan, 2009) and the  $\gamma$  and  $\theta$  were calculated and  
 164 measured using the same method as mentioned above. Due to the fabrication process, the contact  
 165 angles at different locations of the micromodel were different due to the surface roughness even  
 166 though two bonded pieces of glass were of the same material. In addition, the salinity variations  
 167 would further aggravate the fluctuations of contact angles, so the  $\theta$  of CO<sub>2</sub>/brine/glass showed  
 168 greater non-homogeneity at different salinities. As determined by Lenormand-Zhang phase  
 169 diagram (Roland Lenormand et al., 1987; Zhang et al., 2011), the displacement pattern was  
 170 viscous fingering when the brine with different salinities was displaced by CO<sub>2</sub> at the rate of 0.05  
 171 ml/min in the duct with the width of 0.1 mm.

172



173

174 **Figure 2.** Distributions of  $\log M$  and  $\log Ca$  under different injections and salinities in the phase  
 175 diagram for four micromodels: black  $\blacksquare$ , the 0.05 mm wide capillary duct, red  $\blacktriangle$ , the 0.1 mm  
 176 wide capillary duct, blue  $\bullet$ , the homogeneous pore doublet model, green  $\blacklozenge$ , the heterogeneous  
 177 pore doublet model.

178

179

180 **Table 2.** The viscosity of brine  $\mu_l$ , interfacial tension between CO<sub>2</sub> and brine  $\gamma$ , contact angle  $\theta$ ,  
 181 capillary number  $\log Ca$  and viscosity ration  $\log M$  when CO<sub>2</sub> displaced brine with different  
 182 salinities in the 0.1 mm wide capillary duct at the injection flow rate of 0.05 ml/min.

Salinity (mol/l)	0	0.5	1.0	1.5	2.0	2.5
$\mu_l$ (mPa·s)	0.8898	0.9289	0.9699	1.0125	1.0566	1.1018
$\gamma$ (mN/m)	73.628	74.860	76.047	77.190	78.292	79.356
$\theta$ (°)	28.41	19.46	11.99	10.73	- <sup>a</sup>	9.40
Log $Ca$	-4.017	-4.055	-4.078	-4.086	-4.062	-4.100
log $M$	-1.775	-1.794	-1.813	-1.831	-1.850	-1.868

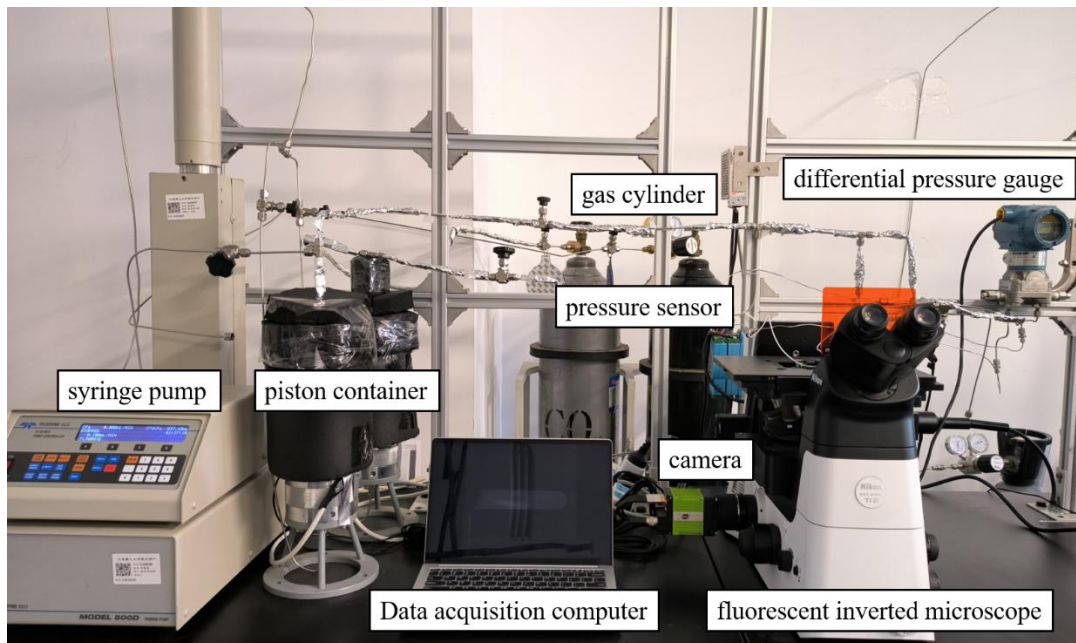
183 <sup>a</sup> Due to the phenomenon of more intense Haines jump, the contact angle could not be  
 184 measured when 2.0 mol/l brine was displaced. But  $\theta=9.67^\circ$  was used to calculate the Log $Ca$  at  
 185 this salinity, which was obtained using an exponential decay model (4) mentioned below.

186

## 187 2.2 Experimental system and procedures

188 The experimental system has been described in detail in the previous publication (Song et  
 189 al., 2020), and the physical diagram is shown in Fig. 3. Two piston containers were connected to  
 190 the same syringe pump (Teledyne ISCO 500D) to control the injection of different fluids in the  
 191 constant flow model. Then they were piped to the inlet of the micromodel and the outlet was  
 192 connected to atmosphere. A differential pressure gauge (Rosemount 3051) measuring from 0 to  
 193 62.2 KPa was connected between the inlet and outlet. The micromodel was placed horizontally  
 194 on a fluorescent inverted microscope (Nikon, ECLIPSE Ti-2U) equipped with a 20 $\times$  lens. A  
 195 camera (SP-12000M-CXP4) was connected to the microscope to capture the entire flow process  
 196 via a data acquisition card (KY-FGK-400).

197



198

199 **Figure 3.** Physical diagram of the experimental system.

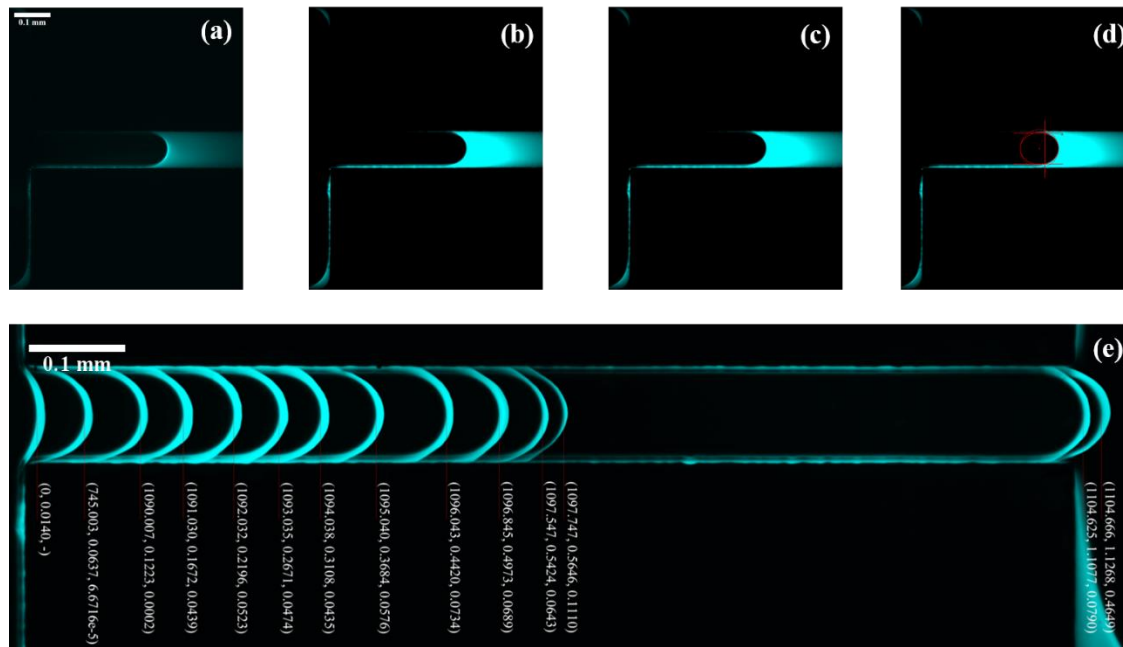
200

201 The entire system needed to be cleaned before all experiments began. Deionized water  
202 (DI), isopropanol, DI and N<sub>2</sub> were used for cleaning in turn, with each fluid injected at a flow  
203 rate of 0.05 ml/min for 2 h to ensure the system was cleaned thoroughly. After the cleaning, the  
204 displacement experiment started. First, the required brine was prepared. Regardless of the  
205 salinity, fluorescent dye (rhodamine B) of 0.2 g/l was added in the brine to distinguish the  
206 aqueous phase from CO<sub>2</sub> and micromodel. Then the dyed brine started to be injected until the  
207 micromodel was fully saturated. To measure the absolute permeability  $K$  of each micromodel,  
208 different injection flow rates, varying from 0.05-0.1 ml/min, were used to achieve the complete  
209 saturation of brine in different experiments. After obtaining the stable differential pressure, the  
210 absolute permeability could be calculated by Darcy's law, as listed in Table 1. Next, the injection  
211 rate was adjusted to the set value, and CO<sub>2</sub> began to be injected to the micromodel. When CO<sub>2</sub>  
212 entered the field of view (FOV), the camera started to capture pictures with fps of 50. Since the  
213 FOV was limited because of the 20× lens, the study was mainly focused on the two-phase flow  
214 near the entrance of the capillary duct or pore doublet model. When the displacement was out of  
215 the FOV, position of micromodel was manually adjusted to better track the two-phase interface.  
216 The displacement was considered to be completed when the differential pressure between the  
217 inlet and outlet remained basically stable and no further changes occurred in the FOV.

### 218 2.3 Image processing

219 The captured images were post-processed mainly using ImageJ and Adobe Photoshop CC  
220 2019. Images at different locations were montaged together into the whole structure through the  
221 relationship between length and pixel using the Photoshop, thus the distribution of different  
222 phases could be obtained in the overall micromodel. ImageJ was mainly used to adjust the  
223 brightness and contrast of the image, so as to better distinguish two phases. Then the noise was  
224 removed, and the saturation of each phase was calculated by adjusting the threshold value. The  
225 specific image processing is shown in Fig. 4. The resolution of images captured in this study was  
226 214.592 nm/pixel. Then the contact angle, velocity field and force field could be obtained  
227 through the processed image. In this study, the contact angle was measured at the interface  
228 curvature using the ellipse fitting, as shown in Fig.4(d). Due to the large capture frequency of the  
229 camera, the velocity field in the capillary duct could be obtained by the position of the interface  
230 at different times, as shown in Fig. 4(e). Due to the limitation of FOV and manual manipulation,  
231 some of the two-phase interface locations in the second half of the capillary duct were not  
232 captured. Finally, the local capillary force, viscosity resistance and total pressure drop between  
233 the entrance and exit of the duct were calculated from the two-phase interface location and the  
234 contact angle at that location.

235



236

237 **Figure 4.** The specific image processing, (a) raw image, (b) image with the brightness and  
 238 contrast adjusted, (c) denoised image, (d) schematic diagram of contact angle measurement, (e)  
 239 montage image, where the numbers in the parenthesis indicate (absolute time (s), distance from  
 240 the two-phase interface to the entrance of the duct (mm), local velocity (m/s)). CO<sub>2</sub> is injected  
 241 from left to right at the rate of 0.002 ml/min and cyan represents the brine.

242

### 243 3 Experimental Results

244 In this study, a total of 21 sets of displacement experiments of CO<sub>2</sub>/brine were conducted.  
 245 Through the experimental measurement and image post-processing, the differential pressure,  
 246 wettability, CO<sub>2</sub> relative permeability, velocity field and force field were obtained to provide  
 247 quantitative analysis for two-phase interface and displacement characteristics at the pore scale.

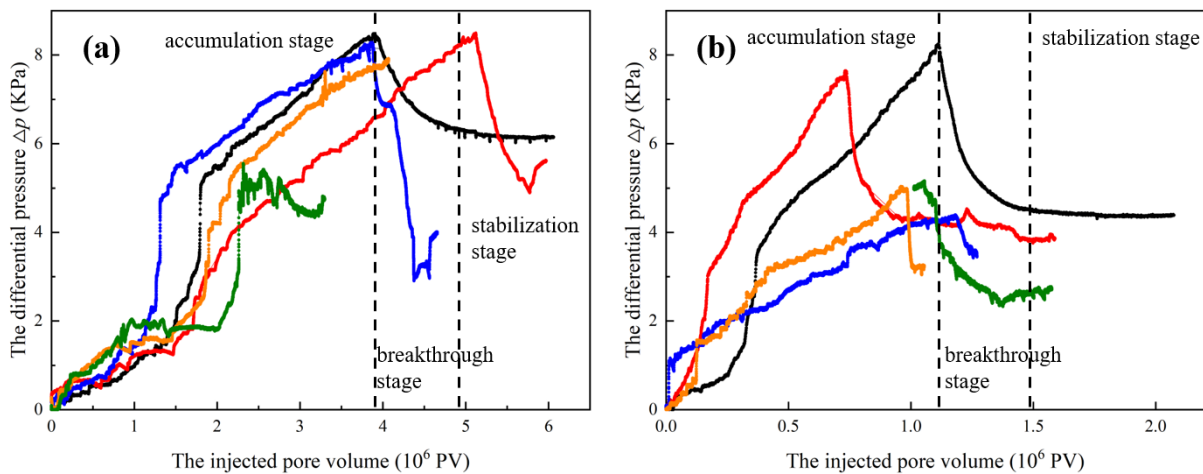
#### 248 3.1 Differential pressure

249 The differential pressure at the inlet and outlet of the micromodel was recorded by  
 250 differential pressure gauge during the entire displacement process, as shown in Fig. 5. The  
 251 differential pressure was consistent with the results of previous study (Jin et al., 2020), and the  
 252 whole process could be roughly divided into three stages: accumulation stage, breakthrough  
 253 stage and stabilization stage, as shown in Fig. 5 when the injection rate was 0.1 ml/min.

254 In the pressure accumulation stage, as the injected PV increased, CO<sub>2</sub> kept accumulating  
 255 at the inlet of the micromodel and was compressed. CO<sub>2</sub> could not displace the brine in the duct  
 256 until the accumulated pressure reached the critical breakthrough pressure  $p_c$ . Whether it was a  
 257 capillary duct or a pore doublet model, the accumulation stage was clearly divided into two  
 258 processes. Pressure built up rapidly when CO<sub>2</sub> was injected from the inlet of the micromodel and  
 259 reached the entrance of the duct through the buffer region. Once CO<sub>2</sub> reached the entrance, the  
 260 build-up rate of pressure decreased and CO<sub>2</sub> started to be compressed, gradually forming a  
 261 curved interface with the aqueous phase. These two different processes of the accumulation stage

262 were approximated as two lines with different slopes, as shown in Fig. 5. When the accumulated  
 263 pressure reached the  $p_c$ , CO<sub>2</sub> started to enter the capillary duct or the pore doublet model to  
 264 displace the brine, and the two-phase interface moved along the flow direction or in the reverse  
 265 direction. As the interface moved forward, the differential pressure decreased until the  
 266 breakthrough. Compared to the accumulation stage, the breakthrough stage proceeded very fast.  
 267 Therefore, the breakthrough time  $t_b$  was defined when differential pressure increased from 0 to  
 268  $p_c$ . For better comparison, the injected PV was used in this study to represent the displacement  
 269 time. After the breakthrough, stability was basically achieved for the differential pressure,  
 270 accompanied with some fluctuations owing to the continuous injection of CO<sub>2</sub>.

271



272

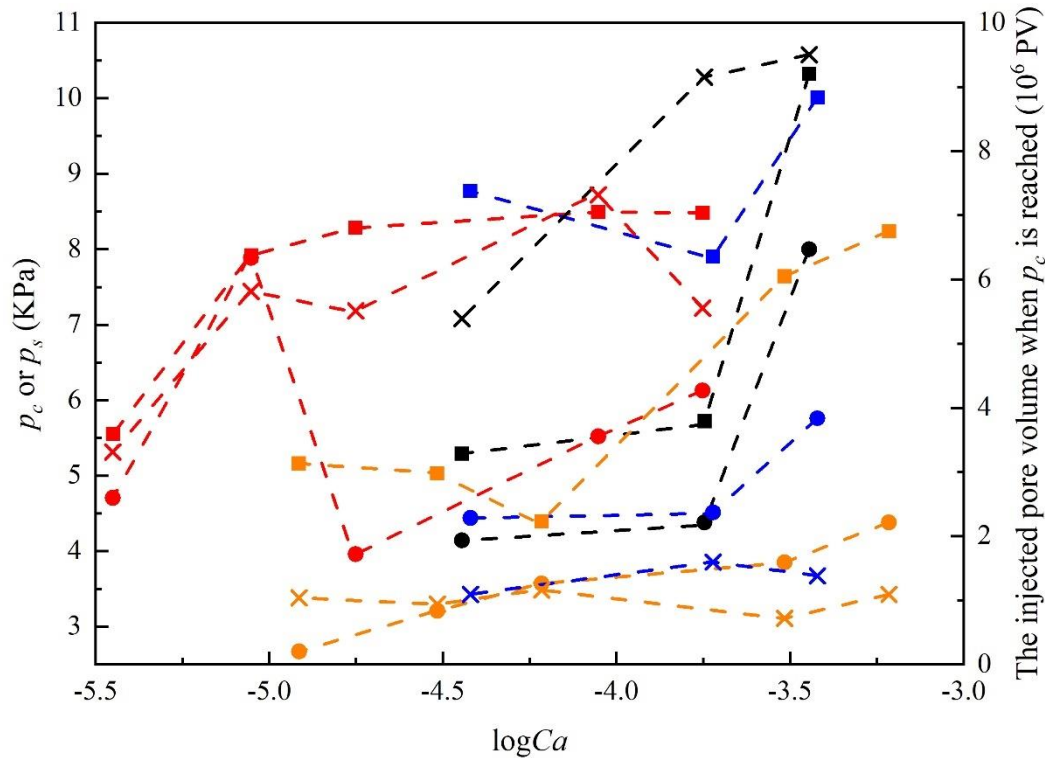
273 **Figure 5.** The development of the differential pressure  $\Delta p$  with the injected pore volume at  
 274 different injection rates marked by lines of different colors: black line-0.1 ml/min, red line-0.05  
 275 ml/min, blue line-0.01 ml/min, orange line-0.005 ml/min, green line-0.002 ml/min, in different  
 276 micromodels: (a) the capillary duct with the width of 0.1 mm, (b) the heterogeneous pore doublet  
 277 model. Two black dotted lines divide the process into three stages in two micromodels at the rate  
 278 of 0.1 ml/min: accumulation stage, breakthrough stage and stabilization stage.

279

280 In general, breakthrough time  $t_b$ , critical pressure  $p_c$  and stabilization pressure  $p_s$  are three  
 281 important characteristic parameters during the displacement. It can be seen from Fig. 5 that these  
 282 three parameters were related to the structure of micromodel and injection flow rate. The  
 283 relationship between these three parameters and capillary numbers in four micromodels is  
 284 summarized in Fig. 6. For the capillary duct, the PV injected to reach the  $p_c$  basically increased  
 285 with  $\log Ca$ , indicating that the increased injection rate does facilitate more CO<sub>2</sub> injection during  
 286 the pressure accumulation stage. In contrast, the PV injected to reach the  $p_c$  in the pore doublet  
 287 model was not much affected by  $\log Ca$ , with the average value  $t_b=1.36 \times 10^6$  PV in the  
 288 homogeneous pore doublet model and  $t_b=0.99 \times 10^6$  PV in the heterogeneous pore doublet model.  
 289 But one thing was consistent with the result in the capillary duct, that was, the increase in width  
 290 decreased the displacement time, i.e., the larger pores and throats will accelerate the process of  
 291 displacement. As for  $p_c$  and  $p_s$ , the value of  $p_s$  was smaller than  $p_c$ , but the trend with  $\log Ca$   
 292 was basically the same. Both pressures increased with the injection rate, which was related to the  
 293 increase of viscous force in the capillary duct or pore doublet model. The difference between  $p_c$

294 and  $p_s$  remained essentially constant in the 0.05 mm wide capillary duct and homogeneous pore  
 295 doublet model. The average value of this difference in the 0.05 mm wide capillary duct was 1.60  
 296 KPa. While in the homogeneous pore doublet model, due to an additional 0.05 mm wide  
 297 capillary duct, this difference doubled to an average value of 3.99 KPa. In the other two  
 298 micromodels, this difference was more complex, partly due to the structure, and partly due to a  
 299 shift of the displacement pattern.

300



301

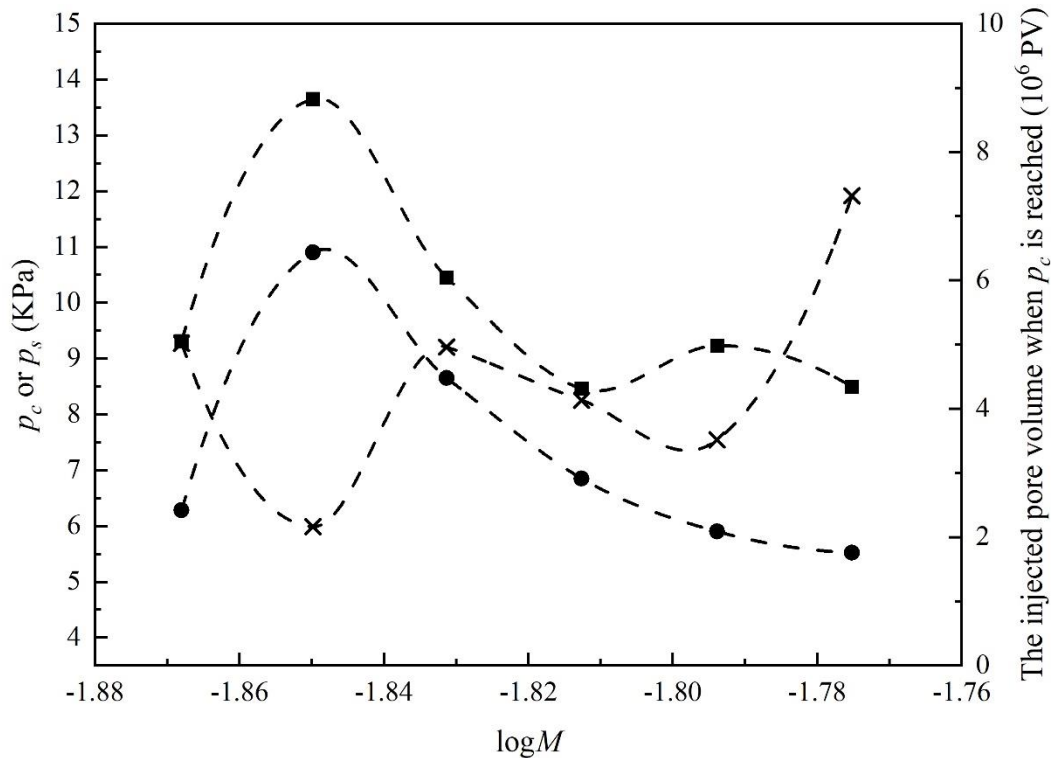
302 **Figure 6.** Variation of the injected pore volume when  $p_c$  is reached ( $\times$ ), maximum differential  
 303 pressure  $p_c$  ( $\blacksquare$ ) and the stabilization differential pressure  $p_s$  ( $\bullet$ ) with  $\log Ca$  in four micromodels  
 304 marked by lines of different colors: black-0.05 mm wide capillary duct, red-0.1 mm wide  
 305 capillary duct, blue-homogeneous pore doublet model, orange-heterogeneous pore doublet  
 306 model.

307

308 The salinity of brine also had an important effect on the differential pressure. From Fig.  
 309 7, it was clear that the effect of salinity on displacement was more complex caused by the  
 310 wettability. Besides direct change in the viscous force, the capillary force was also affected when  
 311  $\text{CO}_2$  displaced brine with different salinities in this study, and the contact angle was an important  
 312 parameter to calculate the capillary force. The roughness of micromodel coupled with the  
 313 salinities of brine led to more complex  $\theta$ , which resulted in larger fluctuation of the capillary  
 314 force to further affect the force field. In the salinity range of 0-2.5 mol/l, the relationship between  
 315 differential pressure and salinity was not significant. Compared to pure water, the presence of  
 316 salinity led to faster breakthrough and larger values of  $p_c$  and  $p_s$ . It can be seen that the variation  
 317 of  $p_c$  and  $p_s$  with salinity was complicated, but the trends were similar. At the salinity of 2.0

318 mol/l, the largest  $p_c$ , the largest  $p_s$  and the fastest breakthrough were achieved, which caused the  
 319 more intense Haines jump that would be described in detail later.

320



321

322 **Figure 7.** Variation of the injected pore volume when  $p_c$  is reached (×), maximum differential  
 323 pressure  $p_c$  (■) and the stabilization differential pressure  $p_s$  (●) with  $\log M$  in the 0.1 mm wide  
 324 capillary duct with  $\text{CO}_2$  injection flow rate of 0.05 ml/min.

325

326 In conclusion, injection flow rate, structure of micromodel and salinity of brine all affect  
 327 the differential pressure during  $\text{CO}_2$  sequestration into the brine aquifer, which is comprehensive  
 328 and complex. Thus, the optimal  $\text{CO}_2$  injection flow rate needs to be determined by considering  
 329 the geological structure and brine mineralization.

### 330 3.2 Contact angle

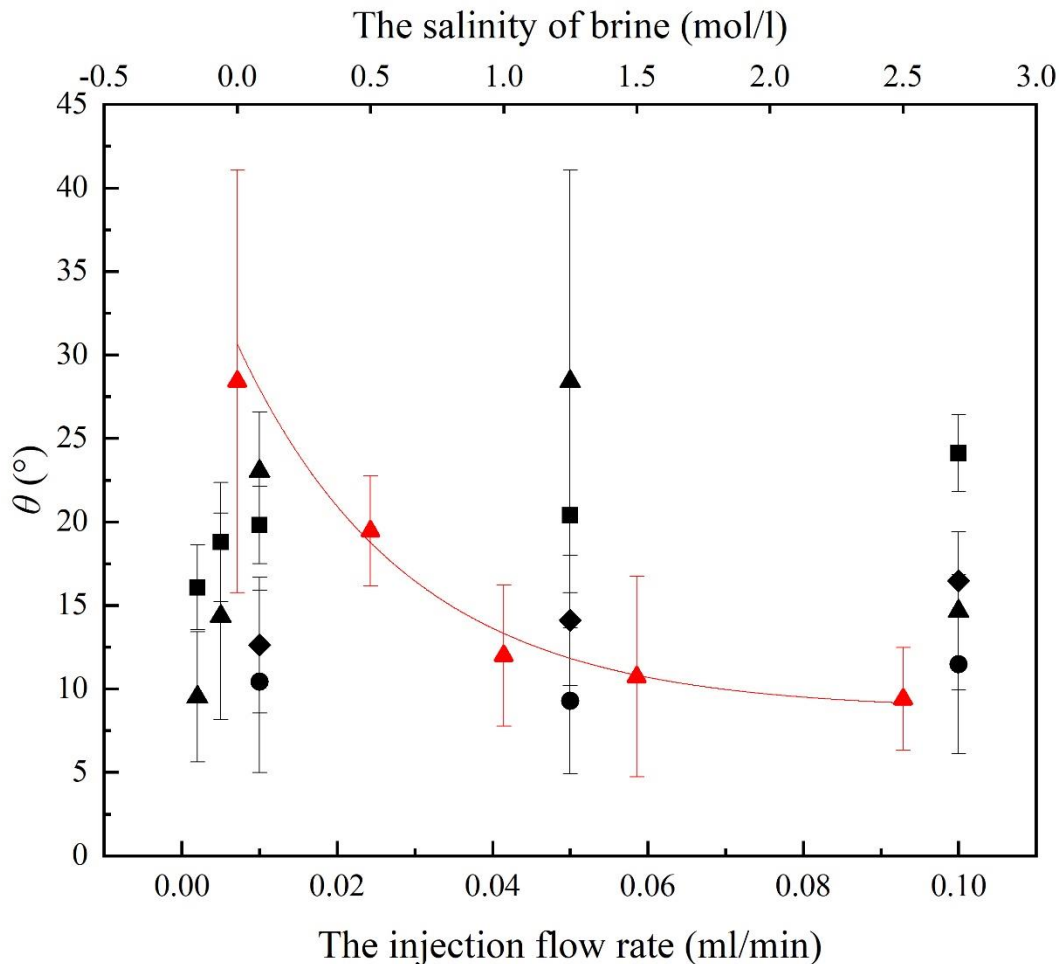
331 Wettability not only affects the capillary number, but also has an important role in the  
 332 capillary force and flow process. Static contact angle is generally used to calculate the capillary  
 333 number, but it has been proved that there is a certain deviation in the static contact angle and  
 334 dynamic contact angle, and even hysteresis between the advancing contact angle and receding  
 335 contact angle (Jafari and Jung, 2019). Therefore, it was more accurate to calculate the  $Ca$  using  
 336 the advancing contact angle in this study. By elliptically fitting the curved interface, advancing  
 337 contact angles at different positions of the same micromodel were measured, and then the contact  
 338 angle used for calculation of  $Ca$  was obtained by averaging advancing contact angles. Due to the  
 339 fabrication, different degrees of roughness existed on the surface of the same micromodel, which  
 340 resulted in different wettability at different locations, as shown in Fig. 8, the standard deviations

341 of the  $\theta$  were relatively large. The average value of the advancing contact angle obtained in this  
 342 study was less than  $30^\circ$  in all four micromodels, so the materials used in this study were  
 343 considered as strongly hydrophilic. It can be seen from Fig. 8 that the average  $\theta$  increased with  
 344 the injection flow rate. The increase in the injection flow rate led to an increase of the viscous  
 345 force, thus reducing the wall hysteresis effect and a smaller equivalent radius of the fitted ellipse,  
 346 which resulted in a larger contact angle. As the salinity of brine increased, the advancing contact  
 347 angle would be inhibited because of the raised intermolecular forces between the brine and  
 348 structure. And this can be quantified by an exponential decay model, which was obtained by  
 349 fitting the experimental data:

$$350 \quad \theta = 8.702 + 20.624e^{\frac{0.040-x}{0.642}} \quad (4)$$

351 where  $x$  was the salinity of brine, and R-Square was 0.97315.

352



353

354 **Figure 8.** Variation of the average advancing contact angle  $\theta$  with standard deviations with the  
 355 injection flow rate and salinity of brine in four micromodels: ●, the 0.05 mm wide capillary  
 356 duct, ▲, the 0.1 mm wide capillary duct (black, as injection rate and red, as salinity), ◆, the  
 357 homogeneous pore doublet model, ■, the heterogeneous pore doublet pore.

358

359 3.3 CO<sub>2</sub> relative permeability

360 CO<sub>2</sub> relative permeability plays an important role in the mobility and migration pathway  
 361 of carbon in the formation. Based on the experimental process and measurement method of this  
 362 study, the CO<sub>2</sub> relative permeability was calculated using formulas proposed by Huang et al  
 363 (Huang Daming, 1984):

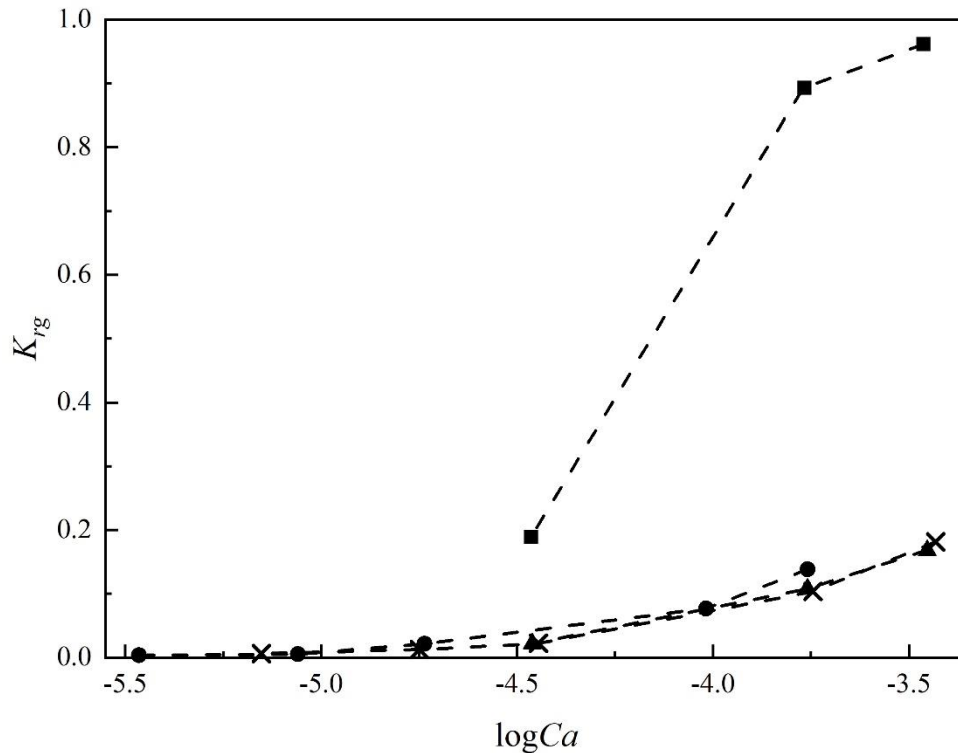
$$K_g = \frac{2LQP_0Z_a\mu_2}{A(P_1^2 - P_2^2)Z_0} \quad (5)$$

364

$$K_{rg} = \frac{K_g}{K} \quad (6)$$

365 Where  $K_g$  is the CO<sub>2</sub> effective permeability,  $K_{rg}$  is the CO<sub>2</sub> relative permeability,  $P_0$  is the  
 366 atmospheric pressure,  $P_1$  is the inlet pressure of the micromodel,  $P_2$  is the outlet pressure of the  
 367 micromodel,  $Z_0$  is the compression coefficient of CO<sub>2</sub> at  $P_0$  and experimental temperature, and  $Z_a$   
 368 is the compression coefficient of CO<sub>2</sub> at the average pressure of  $P_1$  and  $P_2$  and experimental  
 369 temperature. Therefore, CO<sub>2</sub> relative permeability after breakthrough was calculated using  
 370 equations (5) and (6) for four micromodels and different salinities, as shown in Figures 9 and 10.

371



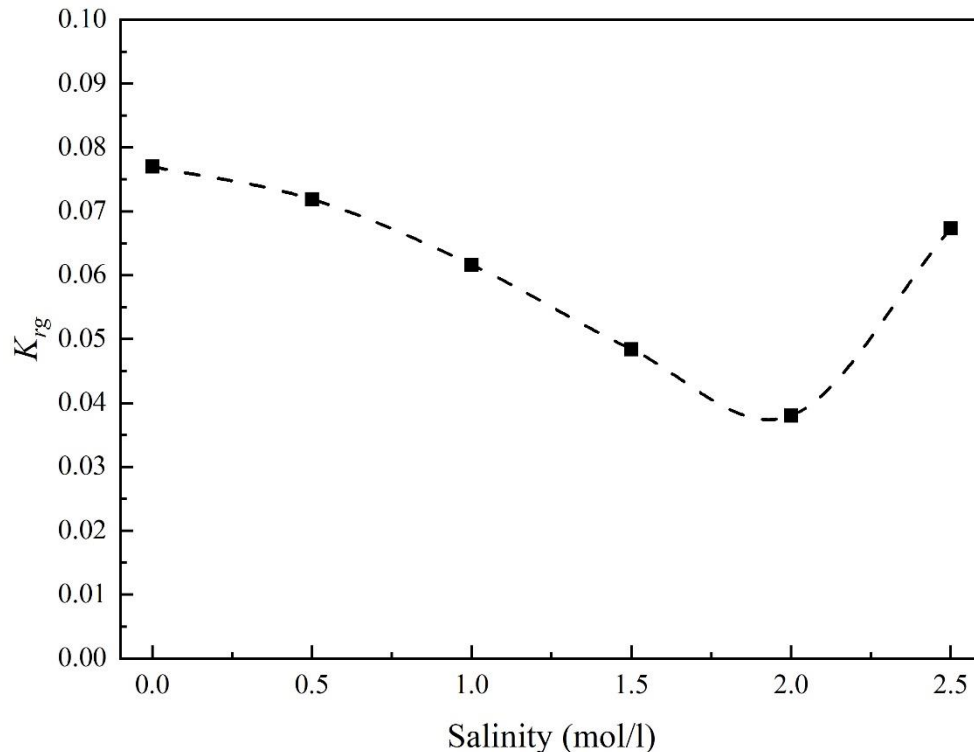
372

373 **Figure 9.** Variation of CO<sub>2</sub> relative permeability  $K_{rg}$  with  $\log Ca$  in four micromodels: ■, the  
 374 0.05 mm wide capillary duct, ●, the 0.1 mm wide capillary duct, ▲, the homogeneous pore  
 375 doublet model, ×, the heterogeneous pore doublet model.

376

377 Consistent with the simulation results of Juanes et al. (Juanes, 2006), CO<sub>2</sub> relative  
 378 permeability would increase with the injection rate. In other words, as the injection rate  
 379 increases, the mobility of injected CO<sub>2</sub> in the formation is enhanced after the displacement, and  
 380 risks of fugitive flow and carbon leakage are more likely to occur. This enhancement was more  
 381 obvious in the 0.05 mm wide capillary duct, which proves that this type of structure was not  
 382 conducive to CO<sub>2</sub> sequestration. The comparison in four micromodels revealed that the CO<sub>2</sub>  
 383 relative permeability would decrease when the width of capillary duct changed from 0.05 mm to  
 384 0.1 mm and the structure changed from capillary duct to pore doublet model. As shown in Fig.  
 385 10, with the presence of salinity, CO<sub>2</sub> relative permeability after the breakthrough would be  
 386 smaller than that obtained when pure water was displaced. This was consistent with the result  
 387 from Bachu et al. (Bachu and Bennion, 2008), who proved it through displacement and  
 388 imbibition experiments with different cores. In the 0.1 mm wide capillary duct, CO<sub>2</sub> relative  
 389 permeability decreased by 50.64% when the displaced phase changed from pure water to 2.0  
 390 mol/l brine. However, CO<sub>2</sub> relative permeability would increase to 0.067 with further increase in  
 391 the salinity (2.5 mol/l in this study), which may be the result of salting out. As shown in Fig. 11,  
 392 salting out occurred near the exit of the capillary duct after the breakthrough when 2.5 mol/l  
 393 brine was displaced by CO<sub>2</sub>. As the salt continued to be precipitated, the width near the exit  
 394 became narrower. As the phenomenon mentioned above, CO<sub>2</sub> relative permeability was greater  
 395 in the narrower capillary duct, so CO<sub>2</sub> relative permeability did not continue to decrease due to  
 396 the salting out when the salinity exceeded 2 mol/l.

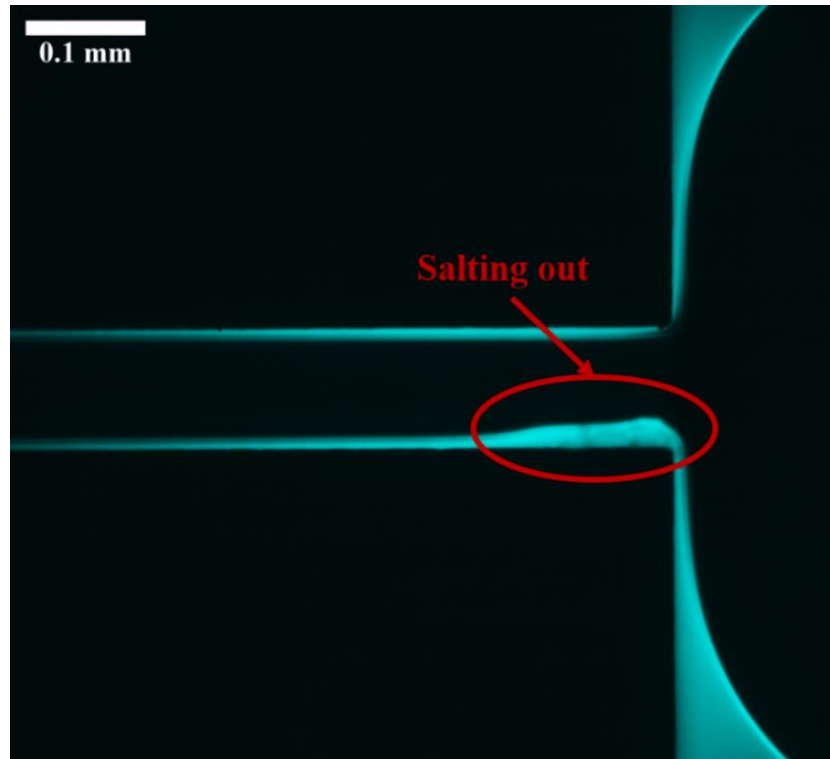
397



398

399 **Figure 10.** Variation of CO<sub>2</sub> relative permeability  $K_{rg}$  with salinity of the brine in the 0.1 mm  
 400 wide capillary duct after the breakthrough with CO<sub>2</sub> injection rate of 0.05 ml/min.

401



402

403 **Figure 11.** Salting out near the exit of the 0.1 mm wide capillary duct after the breakthrough.  
 404 The injection direction is from left to right, and cyan represents the brine with the salinity of 2.5  
 405 mol/l.

406

### 407 3.4 Velocity field

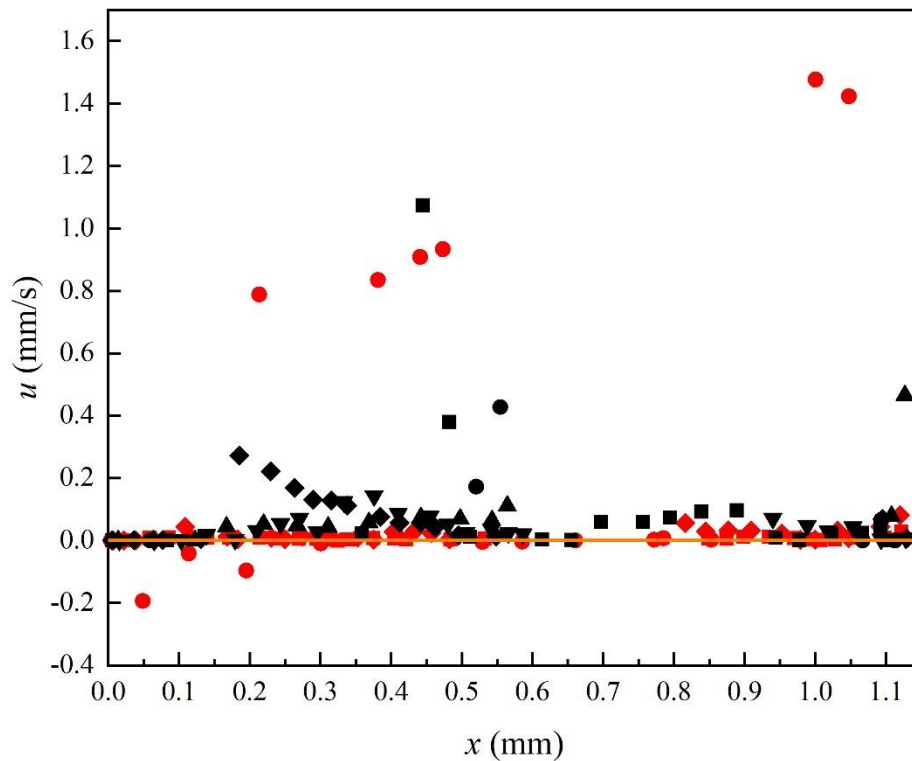
408 In this study, the fps of camera was set to 50, which was sufficient to capture the  
 409 displacement process. The positions of CO<sub>2</sub>/brine interface at different moments were obtained  
 410 from the montaged images, as shown in Fig. 4(e), and the local velocity  $u$  could be calculated  
 411 using the interface distance  $\Delta x$  in the adjacent time  $\Delta t$ :

$$412 \quad u = \frac{\Delta x}{\Delta t} \quad (7)$$

413 The variation of local velocity with the interface position from the entrance of the  
 414 capillary duct under different conditions is shown in Figures 12 and 13. Compared with the bulk  
 415 injection flow rate  $Q$ , as shown in Table 1, the calculated local velocity was about 3 orders of  
 416 magnitude smaller in the capillary duct. As can be seen from Fig. 12, the displacement pattern  
 417 had an important effect on the velocity field. When the injection flow rate was large, the  
 418 displacement pattern was viscous fingering, and the velocity fluctuation in the duct was quite  
 419 great. When the pattern gradually changed to the crossover, the velocity distribution was more  
 420 uniform along the displacement direction. Due to the entrance/exit effect, the local velocity was  
 421 relatively small at the entrance and exit of the capillary duct. An abrupt change in velocity, i.e.,  
 422 Haines jump, would occur in the pattern of viscous fingering, and this phenomenon basically  
 423 occurred in the first half of the capillary duct. In the second half, the viscous force decreased as

424 the reduction of the aqueous phase, thus the pressure drop was not sufficient to generate Haines  
 425 jump. The local velocity  $u$  was negative at some positions in the 0.05 mm wide capillary duct,  
 426 i.e., the backflow of aqueous phase occurred at that position, and the same phenomenon was  
 427 observed when CO<sub>2</sub> displaced the brine with the salinity of 0.0, 1.0 and 1.5 mol/l in the 0.1 mm  
 428 wide capillary duct, as shown in Fig. 13. This will be described in detail in the next section. The  
 429 occurrence of salinity can reinforce the fluctuation of the velocity field, making Haines jump  
 430 more obvious. It was also found that an abrupt increase of velocity to a certain value would be  
 431 maintained for a period of time, but would decrease back to the lower velocity when the pressure  
 432 drop was not sufficient to maintain the higher velocity.

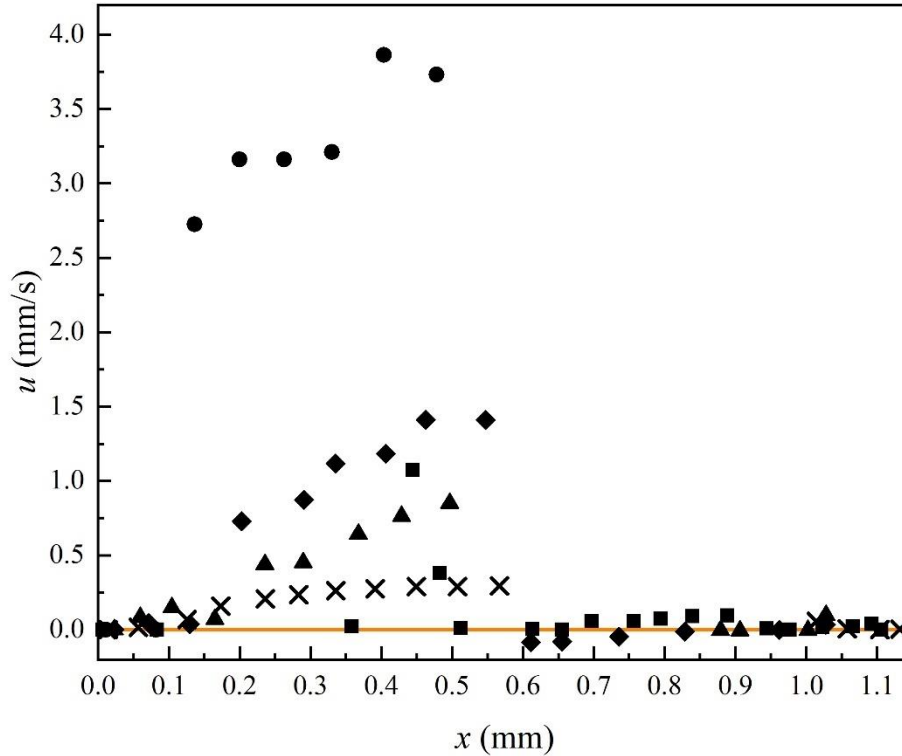
433



434

435 **Figure 12.** The local velocity  $u$  at different interface locations  $x$  from the entrance in the  
 436 capillary duct with the widths of 0.05 mm (marked in red) and 0.1 mm (marked in black) at  
 437 different injection flow rates: ▲, 0.002 ml/min, ▼, 0.005 ml/min, ●, 0.01 ml/min, ■, 0.05  
 438 ml/min, ◆, 0.1 ml/min. The yellow line is the base line with the velocity of 0.

439



440

441 **Figure 13.** The local velocity  $u$  at different interface locations  $x$  from the entrance in the  
 442 capillary duct with the width of 0.1 mm when  $\text{CO}_2$  was injected at the rate of 0.05 ml/min to  
 443 displace the brine with different salinities:  $\blacksquare$ , 0.0 mol/l,  $\bullet$ , 0.5 mol/l,  $\blacktriangle$ , 1.0 mol/l,  $\blacklozenge$ , 1.5 mol/l,  
 444  $\times$ , 2.5 mol/l. The yellow line is the base line with the velocity of 0.

445

446 3.5 Force field

447 The differential pressure measured by differential pressure gauge was not exactly equal to  
 448 the pressure drop between the entrance and exit of the capillary duct or pore doublet model. The  
 449 piping between the differential pressure gauge and micromodel, the buffer zone near the entrance  
 450 and exit and the entrance/exit effect were the main reasons for this difference. Combined with  
 451 the theoretical analysis, the force field in the capillary duct was calculated without considering  
 452 the influence of these factors, as shown in Figures 14 and 15.

453 When immiscible flow occurs in the capillary duct, the overall pressure drop  $\Delta P$   
 454 between the entrance and exit is composed of viscous pressure  $\Delta P_v$  and capillary pressure  $\Delta P_c$ :

455 
$$\Delta P = \Delta P_v + \Delta P_c \quad (8)$$

456 where  $\Delta P_v$  is calculated by the modified Hagen-Poisson flow by Mortensen et  
 457 al.,(Mortensen et al., 2005) where the effect of the shape factor  $\alpha$  is taken into account:

458 
$$\Delta P_v = \alpha \frac{Q\mu L}{A^2} \quad (9)$$

459 where  $\mu$  is the effective viscosity of two fluids in the capillary duct:

460 
$$\mu = \frac{x}{L} \mu_2 + \frac{L-x}{L} \mu_1 \quad (10)$$

461 where  $x$  is the distance from the entrance to two-phase interface. The shape factor  $\alpha$  is  
 462 related to the cross-section of the duct, which is rectangular in this study. The relationship  
 463 between  $\alpha$  and the dimensionless number of shape  $C$  for the rectangular cross-section was  
 464 proposed by Mortensen et al.(Mortensen et al., 2005) as follows:

465 
$$\alpha(C) = \frac{22}{7} C - \frac{65}{3} + O([C-18]^2) \quad (11)$$

466 
$$C = \frac{p^2}{A} \quad (12)$$

467 where  $p$  is the perimeter of the cross-section. Then  $\Delta P_v$  at different interface locations is  
 468 calculated by bringing equations (10)(11)(12) into equation (9).

469 Due to the rectangular cross-section used in this study, the capillary pressure at different  
 470 interface locations was calculated using the modified Young-Laplace equation by Juncker et  
 471 al.(Juncker et al., 2002):

472 
$$P_c = 2\sigma \cos \theta \left( \frac{1}{w} + \frac{1}{d} \right) \quad (13)$$

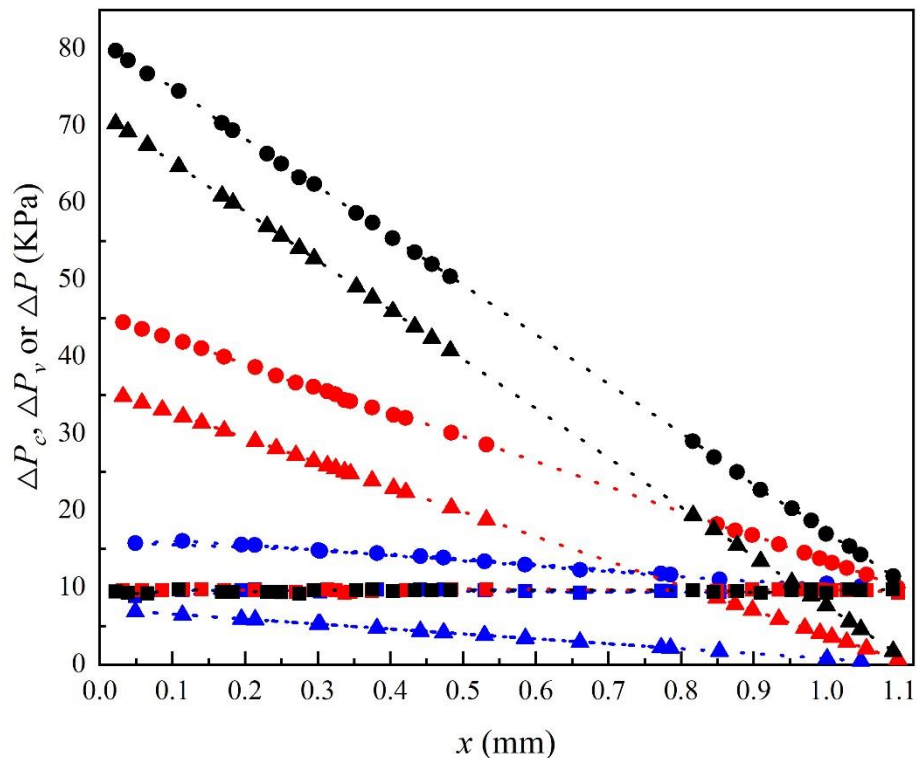
473 Combining equations (9) and (13), the total pressure drop  $\Delta P$  during the displacement  
 474 can be calculated using equation (8), and the fields of three pressures, local capillary force  $\Delta P_c$ ,  
 475 viscous force  $\Delta P_v$  and overall pressure drop  $\Delta P$ , are shown in Figures 14-16. The results  
 476 further confirmed that the two-phase flow was closely related to the width of duct, interface  
 477 location, injection flow rate, contact angle and salinity.

478 In this study, the displacement patterns were viscous fingering and crossover according to  
 479 the phase diagram, thus the viscous force played an important role for the two-phase flow. The  
 480  $\Delta P_v$  decreased linearly as the interface moved toward the exit of the duct. Because the viscosity  
 481 of CO<sub>2</sub> is much less than brine, the  $\Delta P_v$  near the entrance was basically caused by the brine. As  
 482 displacement proceed, the brine was continuously displaced, causing a decrease in the effective  
 483 viscosity. After breakthrough, the viscous force in the duct was essentially from CO<sub>2</sub>. As for the  
 484 capillary force, the heterogeneity of wettability was the main reason for its fluctuation at  
 485 different locations in the same duct. Comparing three pressures in two capillary ducts with  
 486 different widths, it was found that the  $\Delta P$ ,  $\Delta P_v$  and  $\Delta P_c$  were greater in the narrower duct.  
 487 This was why larger injected PV was needed to achieve the displacement in the 0.05 mm wide  
 488 capillary duct.

489 It was found through Figures 14 and 15 that the displacement pattern had a large effect on  
 490 the pressure field. When viscous fingering occurred, the viscous force of the displaced phase  
 491 would be greater than the capillary force and dominated the displacement. But this difference  
 492 gradually decreased as interface moved toward the exit of the duct, and the capillary force would  
 493 be greater than viscous force due to the almost absence of brine near the breakthrough.  
 494 Therefore, there must exist a position where  $\Delta P_v = \Delta P_c$ , and then the displacement pattern  
 495 transformed from viscous fingering to crossover, and as the interface continued to advance, the

496 capillary force dominated and then capillary fingering would occur. As the flow rate increased,  
 497 the location where this pattern shift occurred was closer to the exit. At lower injection rate in this  
 498 study, the crossover occurred near the entrance of the duct, where  $\Delta P_v = \Delta P_c$  or  $\Delta P_v < \Delta P_c$ .  
 499 Capillary fingering would occur as the interface moved toward the exit when the capillary force  
 500 dominated. As can be seen, the viscous force decreased little at lower flow rate, so the  
 501 probability of the displacement pattern shift was small. Even if it did, the position was closer to  
 502 the exit of the duct.

503



504

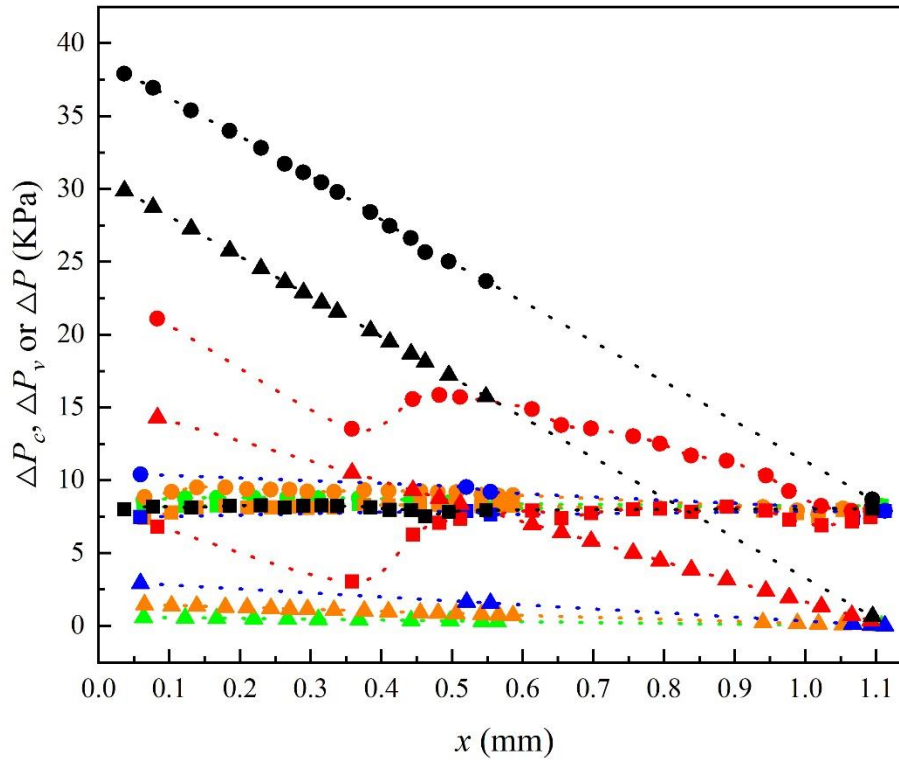
505 **Figure 14.** The local capillary force  $\Delta P_c$  (■), viscous force  $\Delta P_v$  (▲) and overall pressure drop  
 506  $\Delta P$  (●) at different interface locations  $x$  from the entrance at different injection rates: 0.01  
 507 ml/min (marked in blue), 0.05 ml/min (marked in red) and 0.1 ml/min (marked in black) in the  
 508 0.05 mm wide capillary duct.

509

510 The effect of the salinity of brine on the force field is shown in Fig. 16. As the salinity  
 511 increased, the viscous force increased when the interface was near the entrance of the duct, and  
 512 thus the total pressure drop also increased. But the viscous force caused by salinity decayed as  
 513 the two-phase interface moved toward the exit, causing almost same values of  $\Delta P$  at different  
 514 salinities near the exit of the duct. Therefore, in the capillary duct of this study, salinity affected  
 515 the displacement mainly by changing the viscous force near the entrance and had little effect on  
 516 the flow behavior near the exit. Comparing with Figure 7, it can be found that although the  
 517 relationship between salinity and force field was obvious, the variation of measured differential  
 518 pressure with salinity was more complicated. Therefore, it was concluded that the effects of  
 519 pipeline, buffer zone and entrance/exit effect could not be negligible. So, the location and length

520 of the injection wellbore should not be underestimated when CO<sub>2</sub> is injected into the brine  
 521 aquifer, and this is the focus of our next research.

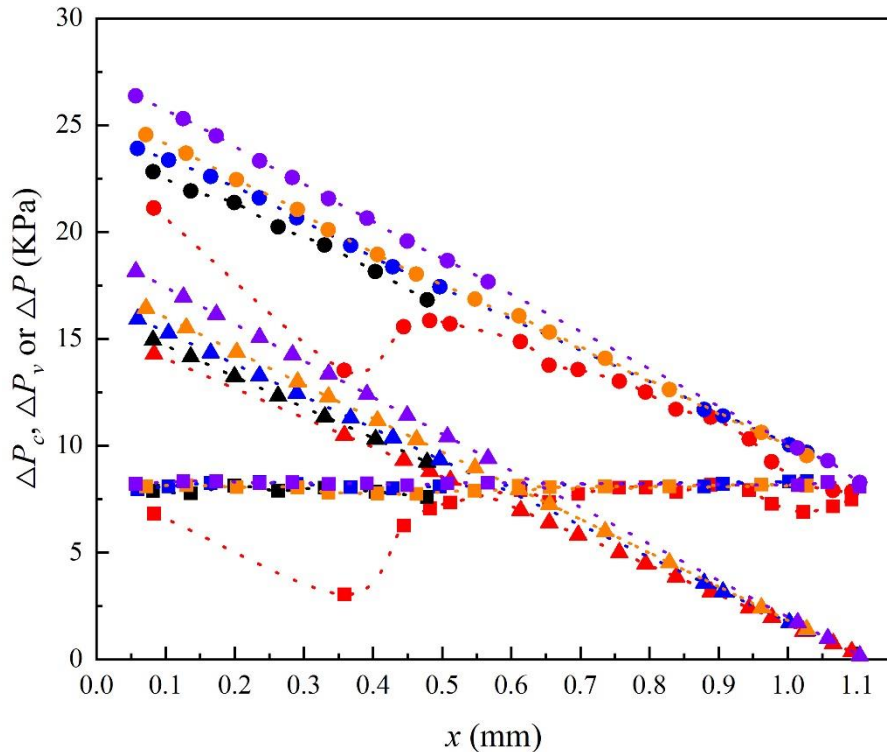
522



523

524 **Figure 15.** The local capillary force  $\Delta P_c$  (■), viscous force  $\Delta P_v$  (▲) and overall pressure drop  
 525  $\Delta P$  (●) at different interface locations  $x$  from the entrance at different injection rates: 0.002  
 526 ml/min (marked in green), 0.005 ml/min (marked in orange), 0.01 ml/min (marked in blue), 0.05  
 527 ml/min (marked in red) and 0.1 ml/min (marked in black) in the 0.1 mm wide capillary duct.

528



529

530 **Figure 16.** The local capillary force (■), viscous force (▲) and overall pressure drop (●) at  
 531 different interface locations  $x$  from the entrance when  $\text{CO}_2$  was injected at 0.05 ml/min to  
 532 displace the brine with different salinities: 0.0 mol/l (marked in red), 0.5 mol/l (marked in black),  
 533 1.0 mol/l (marked in blue), 1.5 mol/l (marked in orange) and 2.5 mol/l (marked in purple) in the  
 534 0.1 mm wide capillary duct.

535

## 536 4 Analysis and Discussion

### 537 4.1 The flow in the capillary duct

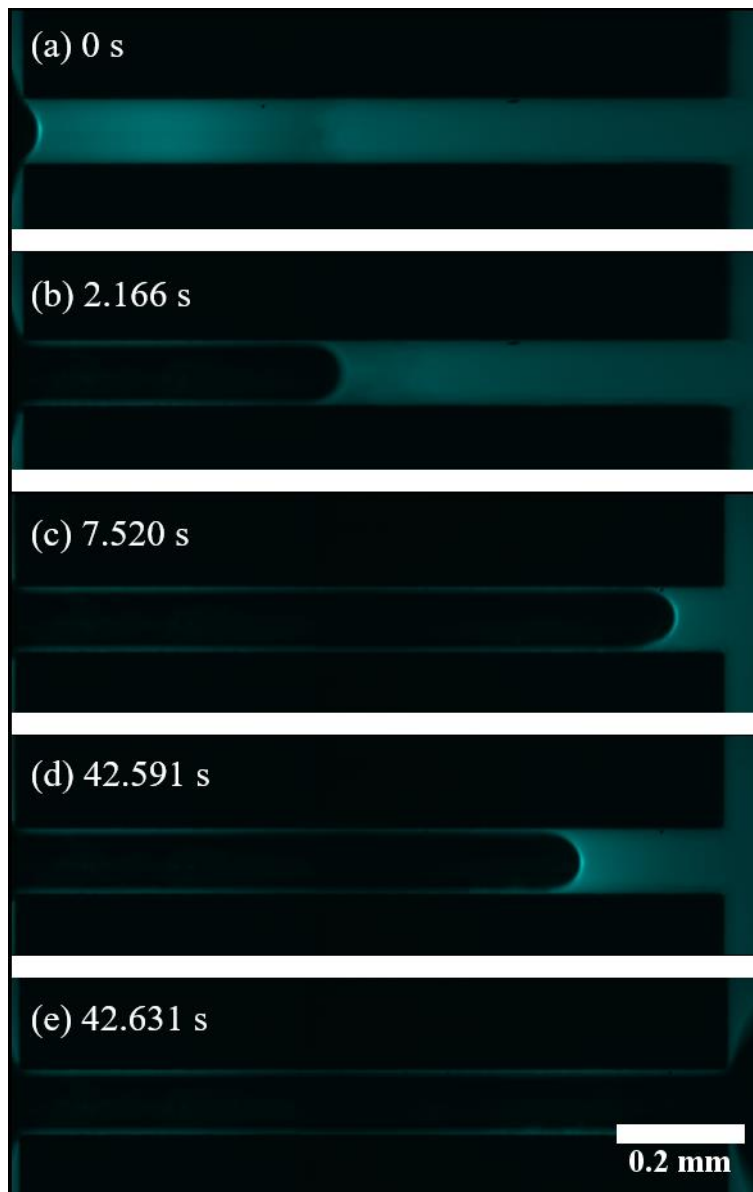
538 The critical pressure to be overcome for  $\text{CO}_2$  to enter the duct would be higher with  
 539 narrower duct and larger injection rate, as described in the force field section. As a result, the  
 540 injected PV and displacement time required from the start of displacement to breakthrough  
 541 increased, and a higher differential pressure was maintained after the breakthrough. So, the large  
 542 injection flow rate, pore and throat are not conducive for the safety of  $\text{CO}_2$  storage into the brine  
 543 aquifer. Although the lower differential pressure after breakthrough at lower injection flow rate  
 544 is favorable for the safety of  $\text{CO}_2$  storage, it takes more time to complete the displacement. In  
 545 terms of economics, it is also inappropriate to use low  $\text{CO}_2$  injection flow rates in practical  
 546 engineering applications. Overall, no matter what duct width and injection flow rate were used,  
 547 breakthrough would always occur in the single capillary duct, and after the breakthrough, the  
 548  $\text{CO}_2$  saturation was basically up to 100% without considering the residual thin films of the  
 549 wetting phase due to the strong hydrophilicity. However, the  $t_b$ ,  $p_c$  and  $p_s$  all varied with the duct  
 550 width and flow rate, and the combined effect of these parameters is critical to the application of  
 551  $\text{CO}_2$  storage into the brine aquifer.

552

553 **Table 3.** The situations when backflow occurred and its location, time and number.

Width of the capillary duct/mm	Salinity of the brine/mol/l	CO <sub>2</sub> injection rate/ml/min	Location of the backflow/mm	Time of the backflow/s	Number of the backflow
0.05	0	0.01	0.7856/0.7726	43.833/1157.886	2
0.05	0	0.05	0.3450	470.007	1
0.1	0	0.01	1.0930	2665.726	1
0.1	1.0	0.05	1.0279	7.520	1
0.1	1.5	0.05	1.0276	17.084	1

554



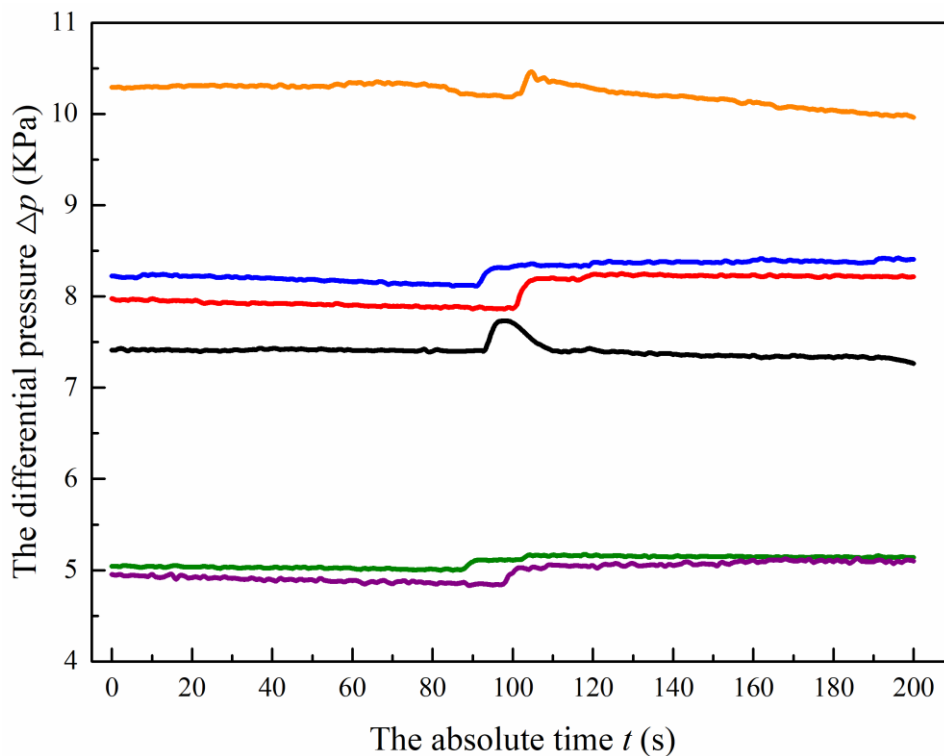
555

556 **Figure 17.** The backflow of wetting phase in the 0.1 mm wide capillary duct when 1.0 mol/l  
 557 brine was displaced by CO<sub>2</sub> at the injection rate of 0.05 ml/min.

558

559 The velocity field showed that the local velocity at some positions was negative, and the  
 560 backflow of wetting phase occurred at this point, as shown in Figure 17. The situations when  
 561 backflow occurred and the corresponding location, time and number are listed in Table 3. Two  
 562 backflows occurred before the final breakthrough when CO<sub>2</sub> was injected at the rate of 0.01  
 563 ml/min in the 0.05 wide capillary duct and the breakthrough was achieved with only one  
 564 backflow in other situations. In general, there was a high probability of backflow when CO<sub>2</sub>  
 565 displaced brine at an intermediate rate, i.e., 0.01 and 0.05 ml/min, in this study. Therefore, there  
 566 was sufficient reason to believe that the displacement at these two injection rates should be  
 567 attributed to crossover, rather than viscous fingering defined in the traditional phase diagram, as  
 568 shown in Fig. 2. Correspondingly, when the injection rate was less than 0.01 ml/min, the  
 569 displacement pattern was capillary fingering instead of crossover. It is demonstrated that  $Ca$  and  
 570  $M$  are not the only parameters to determine the displacement pattern (Bakhshian et al., 2019).

571



572

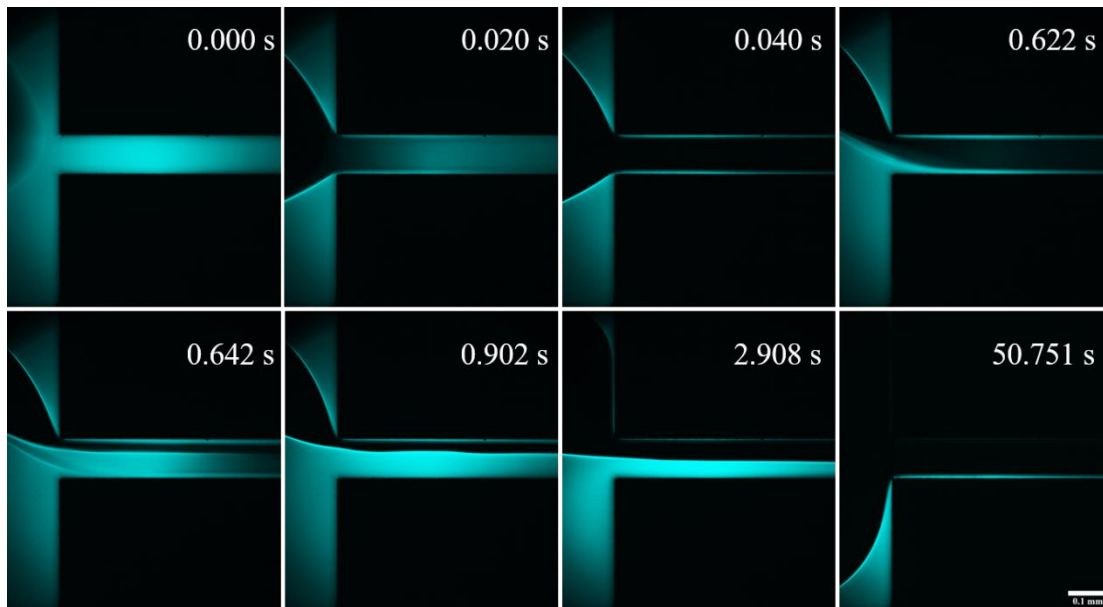
573 **Figure 18.** local differential pressure  $\Delta p$  with the absolute time  $t$  at different conditions marked  
 574 by lines of different colors: black line-2.0 mol/l brine was displaced by CO<sub>2</sub> with the rate of 0.05  
 575 ml/min in the 0.1 mm wide capillary duct, red line-the pure water was displaced by CO<sub>2</sub> with the  
 576 rate of 0.01 ml/min in the 0.1 mm wide capillary duct, blue line-1.0 mol/l brine was displaced by  
 577 CO<sub>2</sub> with the rate of 0.05 ml/min in the 0.1 mm wide capillary duct, orange line-1.5 mol/l brine  
 578 was displaced by CO<sub>2</sub> with the rate of 0.05 ml/min in the 0.1 mm wide capillary duct, green line-  
 579 the pure water was displaced by CO<sub>2</sub> with the rate of 0.01 ml/min in the 0.05 mm wide capillary

580 duct, purple line-the pure water was displaced by CO<sub>2</sub> with the rate of 0.05 ml/min in the 0.05  
 581 mm wide capillary duct.

582

583 The phenomenon of backflow mainly occurred in the second half of the duct where the  
 584 capillary force dominated and it was mainly caused by the fluctuations of the pressure distributed  
 585 along the two-phase interface (Bakhshian et al., 2019). Theoretically, the local velocity  
 586 distribution transverse to the flow direction was symmetric, but the fluctuation caused by  
 587 wettability triggered an imbalance of shear forces along the interface. Thus, this interface moved  
 588 against the direction of injection until the forces rebalanced (Jiamin Wan, 1996). The pressure  
 589 built up again to overcome the flow resistance and achieve the breakthrough. As shown in Fig.  
 590 18, the differential pressure  $\Delta p$  would gradually drop to a value when the backflow occurred,  
 591 and then an abrupt increase would cause Haines jump to achieve the breakthrough.

592



593

594 **Figure 19.** The more intense Haines jump in the 0.1 mm wide capillary duct when 2.0 mol/l  
 595 brine was displaced by CO<sub>2</sub> at the rate of 0.05 ml/min. The camera's fps is 100. The injection  
 596 direction is from left to right. Cyan represents the brine and black represents the CO<sub>2</sub> and  
 597 micromodel skeleton.

598

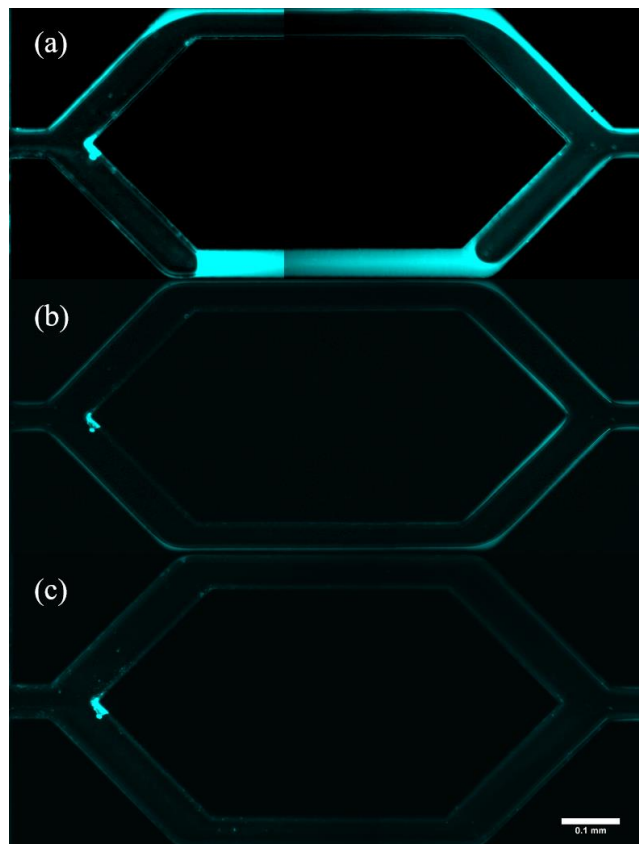
599 In addition, the phenomenon of more intense Haines jump was found in this study, as  
 600 shown in Fig. 19. The brine with the salinity of 2.0 mol/l was quickly displaced by CO<sub>2</sub> at the  
 601 injection rate of 0.05 ml/min in 0.04 s, and it was consistent with the result simulated by Tsuji et  
 602 al.(Tsuji et al., 2015) when the displacement pattern was crossover. In this study, this transient  
 603 process could not be captured due to the limitation of camera's fps (repeated three times with fps  
 604 of 50, 80, 100, respectively). There was an abrupt change of differential pressure to characterize  
 605 this type of Haines jump, as shown in Fig. 18. After this happened, the residual aqueous phase  
 606 near the entrance would enter the duct again during 0.622-0.902 s, as shown in Fig. 19. The brine

607 continued to enter the duct through the film to cause the film thickness to increase, and even  
 608 tended to completely occupy the duct again. Due to the continuous injection of CO<sub>2</sub> and the  
 609 limited amount of residual brine, finally, the aqueous phase in the duct was almost completely  
 610 displaced. This phenomenon cannot be explained by the obtained pressure field in this study and  
 611 needs to be further investigated.

612 4.2 The flow in the pore doublet model

613 Although the fields of velocity and pressure in the pore doublet model are more complex,  
 614 the two-phase flow in the pore doublet model is easy to understand by analogy with the capillary  
 615 duct. Theoretically, in the homogeneous pore doublet model, all three pressures are equal in the  
 616 two ducts with the same width, and CO<sub>2</sub> can displace the water at the same velocity in both  
 617 ducts, and finally two-phase interfaces meet at the exit to achieve the breakthrough (Chatzis and  
 618 Dullien, 1983). In the heterogeneous pore doublet model, the total pressure drop required to  
 619 initiate the displacement in the narrower duct is greater than the other duct due to the greater  
 620 capillary force. Therefore, as CO<sub>2</sub> is injected, the total pressure drop rises to reach the critical  
 621 pressure in the wider duct firstly, where the displacement occurs and breakthrough can be  
 622 achieved. And since the total pressure drop cannot reach the critical pressure in the narrower  
 623 duct, the brine will not be displaced and will remain in that duct. Most of the experimental  
 624 results are in accordance with the theoretical analysis, but some experimental results deviate  
 625 from theoretical analysis for the displacement at lower flow rate in homogeneous pore doublet  
 626 model and higher flow rate in heterogeneous pore doublet model, as shown in Figures 20 and 21.

627



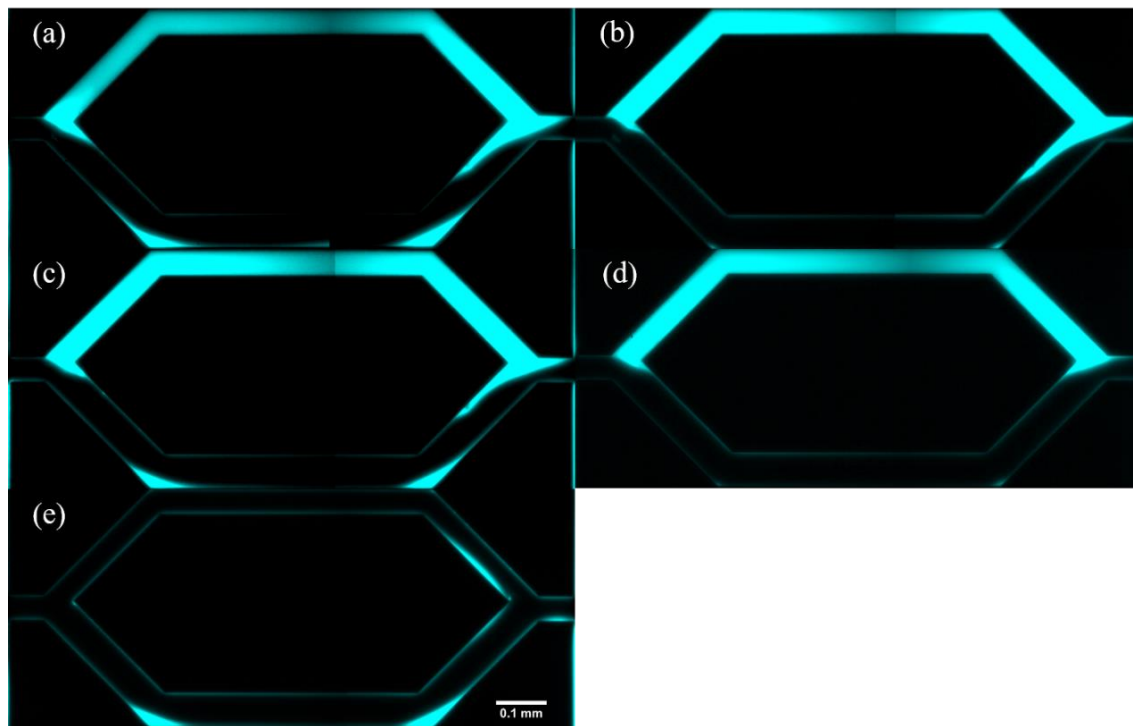
628

629 **Figure 20.** Images of CO<sub>2</sub> and water distributions at the quasi-steady state in the homogeneous  
 630 pore doublet model at different injection rates: (a) 0.01 ml/min, (b) 0.05 ml/min, (c) 0.1 ml/min.  
 631 The injection direction is from left to right. Cyan represents the brine and black represents the  
 632 CO<sub>2</sub> and micromodel skeleton.

633

634 In the homogeneous pore doublet model, when the injection rate was 0.01 ml/min, the  
 635 brine in the upper duct was completely displaced, while only the brine near the entrance and exit  
 636 of the lower duct was displaced, and the residual brine was stabilized between the corners of the  
 637 lower duct, as shown in Fig. 20(a). This was related to the dominance of capillary force at lower  
 638 rate. Although two ducts had the same widths, the critical pressures needed to be overcome were  
 639 different due to the wettability fluctuation caused by the roughness of the micromodel, so the  
 640 displacement would preferentially occur in the duct with the lower critical breakthrough  
 641 pressure. In addition, the corners in the model had an important effect on the two-phase flow. As  
 642 can be seen in Fig. 20, there was an accumulation of aqueous phase and fluorescent dye at the  
 643 corner of the duct bifurcation. At lower injection rate (0.01 ml/min in this study), not only the  
 644 water in the lower duct was trapped between the corners, but a certain amount of water was  
 645 captured at the corners of the upper duct. And the calculated residual saturation of water was  
 646 31.85%. The corner flow was more pronounced in the heterogeneous pore doublet model, as  
 647 shown in Fig. 21.

648



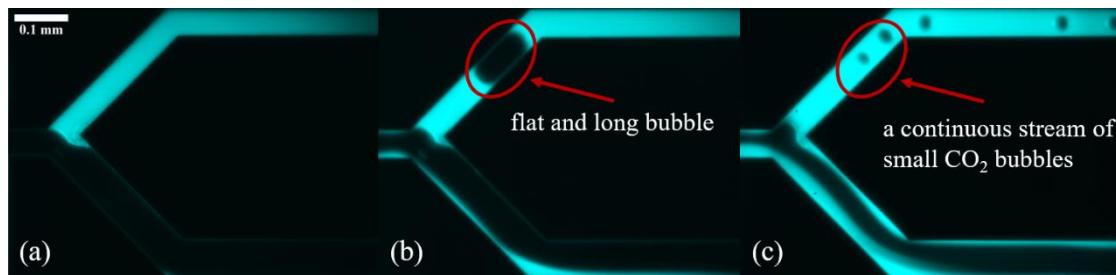
649

650 **Figure 21.** Images of CO<sub>2</sub> and water distributions at the quasi-steady state in the heterogeneous  
 651 pore doublet model at different injection rates: (a) 0.002 ml/min, (b) 0.005 ml/min, (c) 0.01  
 652 ml/min, (d) 0.05 ml/min, (e) 0.1 ml/min. The injection direction is from left to right. Cyan  
 653 represents the brine and black represents the CO<sub>2</sub> and micromodel skeleton.

654

655 The experimental results obtained in the heterogeneous pore doublet model were  
 656 basically in agreement with the theoretical analysis (Chatzis and Dullien, 1983), as shown in Fig.  
 657 21. The water in the wider duct was completely displaced, while the displacement cannot occur  
 658 in the narrower duct. Unlike the homogeneous pore doublet model, the residual wetting phase is  
 659 distributed between the entrance and exit of the model, rather than between the corners of the  
 660 narrower duct. The residual water saturations after the breakthrough were 61.01%, 48.42%,  
 661 55.50% and 46.11% when CO<sub>2</sub> was injected with the rates of 0.002, 0.005, 0.01 and 0.05  
 662 ml/min, respectively. And the fluctuation of saturation was mainly caused by the corner flow.

663



664

665 **Figure 22.** Different mechanisms of trapping water displaced by different forms of CO<sub>2</sub> in the  
 666 heterogeneous pore doublet model at different injection rates: (a) 0.002 ml/min, (b) 0.005  
 667 ml/min, (c) 0.05 ml/min. The injection direction is from left to right. Cyan represents the brine and black  
 668 represents the CO<sub>2</sub> and micromodel skeleton.

669

670 When CO<sub>2</sub> injection rate was 0.002 ml/min, the water in the narrower duct was never  
 671 displaced by CO<sub>2</sub>, and this low injection rate also caused the significant corner stagnation of  
 672 water in wider duct, as shown in Figures 21(a) and 22(a). As the injection rate increased,  
 673 although the water in narrower duct was not displaced after the breakthrough, CO<sub>2</sub> could enter  
 674 this duct during the displacement process. When the CO<sub>2</sub> injection flow rate was 0.005 ml/min,  
 675 CO<sub>2</sub> would enter the narrower duct in the form of flat and long bubbles after the breakthrough in  
 676 the wider duct, as shown in Fig. 22(b). However, this form of CO<sub>2</sub> was unable to displace the  
 677 brine and kept advancing in the aqueous phase to reach the outlet. When the stabilization  
 678 pressure was reached, no more CO<sub>2</sub> bubbles would be produced. When the injection rate  
 679 continued to increase to 0.1 ml/min, a continuous stream of small CO<sub>2</sub> bubbles would form to  
 680 enter the narrower duct after the breakthrough in the wider duct, as shown in Fig. 22(c).  
 681 Macroscopically, the brine could not be displaced as well by the form of continuous stream of  
 682 CO<sub>2</sub> bubbles. Similarly, the CO<sub>2</sub> in bubble form would disappear when the stabilization pressure  
 683 was reached, and then the final two-phase distribution was obtained. At high injection flow rate  
 684 of 0.1 ml/min, the viscous force of water dominated, and the overall pressure drop at the inlet  
 685 was large enough to satisfy the critical pressures required in two ducts with different widths at  
 686 the same time. So, the displacement would occur to achieve the complete CO<sub>2</sub> saturation in both  
 687 ducts simultaneously, as shown in Fig. 21(e). This is instructive for the storage capacity when  
 688 CO<sub>2</sub> is injected into the brine aquifer.

## 689 5 Conclusions

690 CO<sub>2</sub> sequestration into the brine aquifer was researched in this study by conducting  
691 displacement experiments of CO<sub>2</sub>/brine in four micromodels. The effects of the structure of  
692 micromodel, the injection rate of CO<sub>2</sub> and the salinity of brine on the two-phase flow were  
693 investigated. The parameters such as the differential pressure, contact angle, permeability,  
694 velocity field and force field were obtained using the microscopic visualization technique and  
695 image processing methods to discuss the displacement behavior in the capillary duct or pore  
696 doublet model.

697 Three important characteristic parameters: breakthrough time, critical pressure and  
698 stabilization pressure were summarized by analyzing the differential pressure. The materials used  
699 in this study were strongly hydrophilic through the measurement of advancing contact angle,  
700 which increased with increasing injection flow rate and decreasing salinity. CO<sub>2</sub> relative  
701 permeability increased with the injection rate and this relationship was stronger in the narrower  
702 duct. Conversely, the increase in the width of capillary duct and the number of ducts would  
703 decrease CO<sub>2</sub> relative permeability. The effect of salinity on CO<sub>2</sub> relative permeability was more  
704 complex due to the salting out. The local velocity was about 3 orders of magnitude smaller than  
705 the bulk injection velocity, and the velocity field was affected by the displacement pattern. The  
706 force field in the capillary duct proved that the displacement pattern was not constant during the  
707 flow.

708 These characteristic parameters were combined to analyze the two-phase flow in the  
709 capillary duct and pore doublet model. The backflow of brine was observed when it was  
710 displaced by CO<sub>2</sub> at the rate of 0.01 and 0.05 ml/min and the more tense Haines jump was found  
711 in the 0.1 mm wide duct when 2.0 mol/l brine was displaced by CO<sub>2</sub> at 0.05 ml/min injection  
712 rate. In the homogeneous pore doublet model, the water could be completely displaced in both  
713 ducts, and when the injection rate decreased, part of the water would be trapped. In the  
714 heterogeneous pore doublet model, the water was completely displaced only in the wider duct,  
715 while the water in the narrower duct was trapped at lower injection flow rate through different  
716 trapping mechanisms: completely non-displaced, flat and long bubbles, continuous stream of  
717 small bubbles. However, the water in two ducts could be completely displaced in the  
718 heterogenous pore doublet model at higher injection rate.

## 719 Acknowledgments

720 This work was supported by the National Natural Science Foundation of China (Grant  
721 51976024), LiaoNing Revitalization Talents Program (Grant XLYC2007117) and the  
722 Fundamental Research Funds for the Central Universities (Grant DUT21LAB104).

## 723 References

- 724 NIST, edited, <http://webbook.nist.gov/chemistry/fluid/>.
- 725 Bachu, S., and B. Bennion (2008), Effects of in-situ conditions on relative permeability  
726 characteristics of CO<sub>2</sub>-brine systems, *Environmental Geology*, 54(8), 1707-1722.

- 727 Bai, M., L. Liu, C. Li, and K. Song (2020), Relative Permeability Characteristics During Carbon  
728 Capture and Sequestration Process in Low-Permeable Reservoirs, *Materials* (Basel), 13(4).
- 729 Bakhshian, S., S. A. Hosseini, and N. Shokri (2019), Pore-scale characteristics of multiphase flow  
730 in heterogeneous porous media using the lattice Boltzmann method, *Sci Rep*, 9(1), 3377.
- 731 Berejnov, V., N. Djilali, and D. Sinton (2008), Lab-on-chip methodologies for the study of  
732 transport in porous media: energy applications, *Lab Chip*, 8(5), 689-693.
- 733 Chang, C., Q. Zhou, J. Guo, and Q. Yu (2014), Supercritical CO<sub>2</sub> dissolution and mass transfer in  
734 low-permeability sandstone: Effect of concentration difference in water-flood experiments,  
735 *International Journal of Greenhouse Gas Control*, 28, 328-342.
- 736 Chang, C., Q. Zhou, M. Oostrom, T. J. Kneafsey, and H. Mehta (2017), Pore-scale supercritical  
737 CO<sub>2</sub> dissolution and mass transfer under drainage conditions, *Advances in Water Resources*, 100,  
738 14-25.
- 739 Chang, C., T. J. Kneafsey, Q. Zhou, M. Oostrom, and Y. Ju (2019), Scaling the impacts of pore-  
740 scale characteristics on unstable supercritical CO<sub>2</sub>-water drainage using a complete capillary  
741 number, *International Journal of Greenhouse Gas Control*, 86, 11-21.
- 742 Chang, C., T. J. Kneafsey, J. Wan, T. K. Tokunaga, and S. Nakagawa (2020), Impacts of Mixed-  
743 Wettability on Brine Drainage and Supercritical CO<sub>2</sub> Storage Efficiency in a 2.5-D Heterogeneous  
744 Micromodel, *Water Resources Research*, 56(7).
- 745 Chang, C., Q. Zhou, T. J. Kneafsey, M. Oostrom, T. W. Wietsma, and Q. Yu (2016), Pore-scale  
746 supercritical CO<sub>2</sub> dissolution and mass transfer under imbibition conditions, *Advances in Water  
747 Resources*, 92, 142-158.
- 748 Chatzis, I., and F. Dullien (1983), Dynamic immiscible displacement mechanisms in pore  
749 doublets: Theory versus experiment, *Journal of Colloid & Interface Science*, 91(1), 199-222.

750 Chen, X., A. Kianinejad, and D. A. DiCarlo (2016), An extended JBN method of determining  
751 unsteady-state two-phase relative permeability, *Water Resources Research*, 52(10), 8374-8383.

752 Gaol, C. L., J. Wegner, and L. Ganzer (2020), Real structure micromodels based on reservoir rocks  
753 for enhanced oil recovery (EOR) applications, *Lab Chip*.

754 Huang Daming, T. Z., Ge Chuanding, Wang Yuying, Sun Chuanmei (1984), Gas-water relative  
755 permeability of low permeability cores measured by stabilization method, *Natural Gas Industry*,  
756 4(2), 25-30.

757 Jafari, M., and J. Jung (2017), Direct Measurement of Static and Dynamic Contact Angles Using  
758 a Random Micromodel Considering Geological CO<sub>2</sub> Sequestration, *Sustainability*, 9(12), 2352.

759 Jafari, M., and J. Jung (2019), Salinity effect on micro-scale contact angles using a 2D micromodel  
760 for geological carbon dioxide sequestration, *Journal of Petroleum Science and Engineering*, 178,  
761 152-161.

762 Jiamin Wan, T. K. T., Chin-Fu Tsang, and Gudmundur S. Bodvarsson (1996), Improved Glass  
763 Micromodel Methods for Studies of Flow and Transport in Fractured Porous Media, *Water*  
764 *Resources Research*, 32(7), 1955-1964.

765 Jin, X., C. Chao, K. Wu, C. Xia, and X. Fan (2020), The effect of CO<sub>2</sub> phase on drainage process  
766 by analysis of transient differential pressure, *Chemical Engineering Science*, 218, 115581.

767 Juanes, R. (2006), Impact of relative permeability hysteresis on geological CO<sub>2</sub> storage, *Water*  
768 *Resources Research*, 42(12).

769 Juncker, D., H. Schmid, U. Drechsler, H. Wolf, M. Wolf, B. Michel, N. de Rooij, and E.  
770 Delamarche (2002), Autonomous Microfluidic Capillary System, *Analytical Chemistry*, 74(24),  
771 6139-6144.

- 772 Kazemifar, F., G. Blois, D. C. Kyritsis, and K. T. Christensen (2015), A methodology for velocity  
773 field measurement in multiphase high-pressure flow of CO<sub>2</sub> and water in micromodels, *Water*  
774 *Resources Research*, 51(4), 3017.
- 775 Kazemifar, F., G. Blois, D. C. Kyritsis, and K. T. Christensen (2016), Quantifying the flow  
776 dynamics of supercritical CO<sub>2</sub>-water displacement in a 2D porous micromodel using fluorescent  
777 microscopy and microscopic PIV, *Advances in Water Resources*, 95, 352-368.
- 778 Lenormand, R., and C. Zarcone (1985), Invasion percolation in an etched network: Measurement  
779 of a fractal dimension, *Phys Rev Lett*, 54(20), 2226-2229.
- 780 Lenormand, R., C. Zarcone, and A. Sarr (1983), Mechanisms of the displacement of one fluid by  
781 another in a network of capillary ducts, *Journal of Fluid Mechanics*, 135(135), 337-353.
- 782 Lenormand, R., E. Touboul, and C. Zarcone (1987), Numerical models and experiments on  
783 immiscible displacements in porous media, *Journal of Fluid Mechanics*, 189(-1), 165.
- 784 Li, Z., S. Wang, S. Li, W. Liu, B. Li, and Q.-C. Lv (2013), Accurate Determination of the CO<sub>2</sub>-  
785 Brine Interfacial Tension Using Graphical Alternating Conditional Expectation, *Energy & Fuels*,  
786 28(1), 624-635.
- 787 M. Dong, I. C. (1995), The imbibition and flow of a wetting liquid along the corners of a square  
788 capillary tube, *Journal of Colloid and Interface Science*, 172, 278-288.
- 789 Mao, S., and Z. Duan (2009), The Viscosity of Aqueous Alkali-Chloride Solutions up to 623 K,  
790 1,000 bar, and High Ionic Strength, *International Journal of Thermophysics*, 30(5), 1510-1523.
- 791 Morais, S., N. Liu, A. Diouf, D. Bernard, C. Lecoutre, Y. Garrabos, and S. Marre (2016),  
792 Monitoring CO<sub>2</sub> invasion processes at the pore scale using geological labs on chip, *Lab Chip*,  
793 16(18), 3493-3502.

- 794 Mortensen, N. A., F. Okkels, and H. Bruus (2005), Reexamination of Hagen-Poiseuille flow: shape  
795 dependence of the hydraulic resistance in microchannels, *Phys Rev E Stat Nonlin Soft Matter*  
796 *Phys*, 71(5 Pt 2), 057301.
- 797 Patmonoaji, A., M. Muharrik, Y. Hu, C. Zhang, and T. Suekane (2020), Three-dimensional  
798 fingering structures in immiscible flow at the crossover from viscous to capillary fingering,  
799 *International Journal of Multiphase Flow*, 122, 103147.
- 800 Sell, A., H. Fadaei, M. Kim, and D. Sinton (2013), Measurement of CO<sub>2</sub> diffusivity for carbon  
801 sequestration: a microfluidic approach for reservoir-specific analysis, *Environ Sci Technol*, 47(1),  
802 71-78.
- 803 Song, Y., C. Zhao, M. Chen, Y. Chi, Y. Zhang, and J. Zhao (2020), Pore-scale visualization study  
804 on CO<sub>2</sub> displacement of brine in micromodels with circular and square cross sections, *International*  
805 *Journal of Greenhouse Gas Control*, 95.
- 806 Tsuji, Takeshi, Matsuoka, Toshifumi, Yamabe, Hirotsu, Liang, and Yunfeng (2015), Lattice  
807 Boltzmann Simulations of Supercritical CO<sub>2</sub>-Water Drainage Displacement in Porous Media: CO<sub>2</sub>  
808 Saturation and Displacement Mechanism, *Environmental Science & Technology: ES&T*, 49(1),  
809 537-543.
- 810 Werth, C. J., C. Zhang, M. L. Brusseau, M. Oostrom, and T. Baumann (2010), A review of non-  
811 invasive imaging methods and applications in contaminant hydrogeology research, *J Contam*  
812 *Hydrol*, 113(1-4), 1-24.
- 813 Wu, M., F. Xiao, R. M. Johnson-Paben, S. T. Retterer, X. Yin, and K. B. Neeves (2012), Single-  
814 and two-phase flow in microfluidic porous media analogs based on Voronoi tessellation, *Lab Chip*,  
815 12(2), 253-261.

816 Zhang, C., M. Oostrom, T. W. Wietsma, J. W. Grate, and M. G. Warner (2011), Influence of  
817 Viscous and Capillary Forces on Immiscible Fluid Displacement: Pore-Scale Experimental Study  
818 in a Water-Wet Micromodel Demonstrating Viscous and Capillary Fingering, *Energy & Fuels*,  
819 25(8), 3493-3505.

820 Zhu, Y., and K. Petkovic-Duran (2009), Capillary flow in microchannels, *Microfluidics and*  
821 *Nanofluidics*, 8(2), 275-282.

822